# Chapter 4

# Detector Description

# Contents


**4 Detector Description** **1**

4.1 Detector Overview . . . 4
4.2 The C0 Experimental Area . . . 6
4.3 BTeV Analysis Magnet . . . 7
4.4 Pixel Vertex Detector . . . 11
4.4.1 Introduction . . . 11
4.4.2 Overview of Vertex Detector . . . 11
4.4.3 Spatial Resolution . . . 12
4.4.4 Pattern Recognition Capability . . . 14
4.4.5 Radiation Hardness . . . 15
4.4.6 Material Thinness . . . 16
4.4.7 Readout Speed . . . 17
4.4.8 Physics Capability . . . 17
4.4.9 Summary . . . 18
4.5 Forward Tracking System . . . 20
4.5.1 Introduction . . . 20
4.5.2 Forward Silicon Tracker . . . 24
4.5.3 Forward Straw Tracker . . . 27
4.6 Charged Particle Identification . . . 30
4.6.1 Requirements . . . 30
4.6.2 RICH radiators . . . 30
4.6.3 RICH dimensions . . . 32
4.6.4 Photo-detectors . . . 36
4.6.5 Expected physics performance . . . 37
4.7 Electromagnetic Calorimeter . . . 40
4.7.1 Introduction . . . 40
4.7.2 Description of the BTeV Calorimeter . . . 40
4.7.3 Radiation Levels and Radiation Tolerance . . . 42
4.7.4 Expected Resolution . . . 44
4.7.5 Examples: Efficiencies in $B^o \to K^*\gamma$ and $B^o \to \rho\pi$ . . . 44
4.7.6 Crystal Acquisition . . . 46
4.8 Muon Detector . . . 49

4.9 General Design Considerations . . . . . 49
4.10 Baseline Muon System . . . . . 50
4.10.1 Baseline Geometry . . . . . 51
4.10.2 Baseline Detector . . . . . 52
4.10.3 Front-end Electronics . . . . . 55
4.11 Trigger Studies . . . . . 55
4.11.1 Properties of additional "noise" hits . . . . . 55
4.11.2 A muon "tracking" trigger . . . . . 56
4.11.3 Muon Trigger Summary . . . . . 58
4.12 The BTeV Trigger System . . . . . 60
4.12.1 Trigger Overview . . . . . 61
4.12.2 Level 1 Vertex Trigger Algorithm . . . . . 62
4.12.3 Level 1 Vertex Trigger Hardware . . . . . 63
4.12.4 Levels 2/3 . . . . . 63
4.13 Data Acquisition System . . . . . 65
4.13.1 Data Movement between Front End Electronics Boards and Buffer Memories . . . . . 65
4.13.2 Data Buffering for the Level 1 Trigger . . . . . 65
4.13.3 Data Buffering and Movement from the Level 1 to Level 2/3 Trigger . 66
4.13.4 Data Logging: Movement of Data from the Level 2/3 Processors to Mass Storage Systems . . . . . 67
4.13.5 Slow Control and Monitoring, Hardware Management, and Parameter Control . . . . . 68

## 4.1 Detector Overview

A schematic of the detector was given in chapter 3. Figure 4.1 gives a layout with more mechanical detail such as a profile of the analysis magnet and its coils, the vacuum pipes and flanges, etc. The best way to understand the detector is to follow what happens to a charged particle produced in a proton-antiproton collision near the center of the C0 Interaction Region (IR) traveling into the instrumented arm. Below, we give a brief description of its trip. We also describe briefly two important elements of BTeV: the trigger and the data acquisition system. In the following subsections, each detector element the particle traverses is discussed with enough detail to explain how it contributes to the physics capability of BTeV.

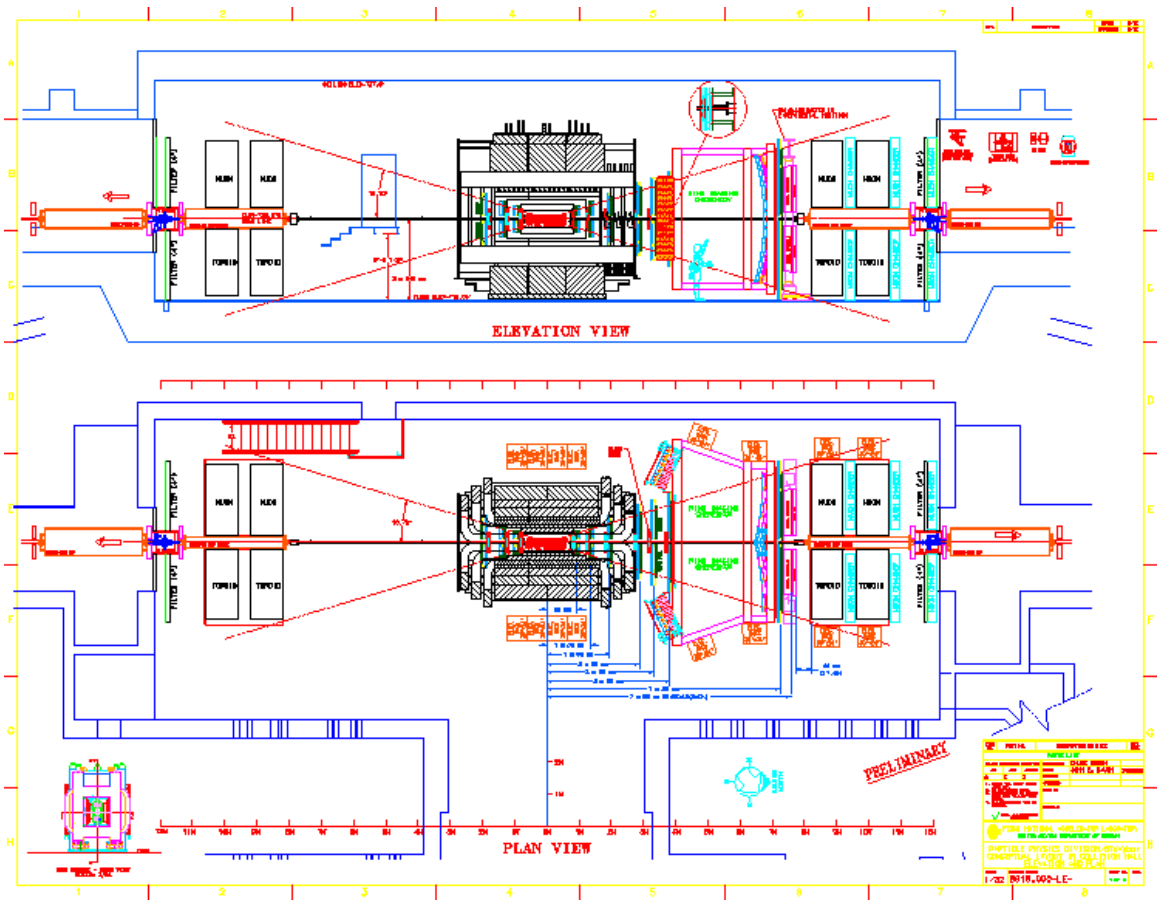


Figure 4.1: Layout of Phase 1 BTeV/C0 Detector – anti-Proton Arm Instrumented

The particle is produced near the middle of the BTeV analysis magnet, which is centered on the IR. The magnet deflects the particle vertically with a field of approximately 1.5 T. The first detector it intercepts is the silicon pixel detector which is inside the magnet. The detector is centered on the IR and has a total of 30 "doublets" of pixel planes, oriented perpendicular to the beam. Each doublet consists of two planes of pixels of 50 $\mu$m$\times$400

$\mu$m. One plane of each doublet has the high precision dimension of the pixel oriented to measure the horizontal coordinate of the track and the other plane has the high precision dimension oriented to measure the vertical coordinate of the track. The high precision tracking permits us to cleanly separate primary interaction vertices from secondary and tertiary vertices associated with $B$ decays. The measurement of the separation, L, has a resolution of about 140 $\mu$m, compared to an average separation of about 4000 $\mu$m for a $B$ decay. Another way to look at this is that we measure the decay proper time with a resolution of about 45 fs, compared to a typical $B$ hadron lifetime of over 1500 fs.

After passing through the pixel planes, the tracks pass through the first six "stations" of the "forward trackers." The first three are in the analysis magnet. The next three are in the relatively low field region downstream of the analysis magnet. These chambers measure the track after it has passed through all of the magnetic field. The forward tracker improves the momentum resolution with respect to the measurement using the pixel detector alone and provides us with excellent mass resolution for $B$ decay candidates. It also serves to confirm that the track enters the Ring Imaging Cherenkov counter (RICH) and provides the best measurement of the coordinates of the particle within it. The forward tracker consists of two sections, an "inner" section of silicon microstrips in the high occupancy region near the beam and an "outer" section of straw tubes in the lower occupancy region at larger angles with respect to the beam.

The particle next enters the RICH, where it encounters first the 1 cm thick liquid-freon, followed by 3 m of gaseous-freon radiator. Cherenkov photons generated in the liquid pass into the gas volume of the RICH and are detected in photomultipliers arrayed along the outside of the gas containment vessel. The Cherenkov photons generated in the gas travel forward to a spherical mirror at the downstream end of the gas volume. The mirror reflects the photons towards the upstream face of the RICH and sideways out of the spectrometer's aperture, and focuses them on arrays of Hybrid Photodiodes. The two RICH systems provide charged particle identification over the energy range from 3-70 GeV/c.

The particle then traverses the 7th station of the forward tracker. This station confirms that the particle traversed the RICH and helps determine its position and angle at the RICH mirror. It also defines the trajectory of the charged particle as it moves towards the most downstream elements of the spectrometer.

Next, the particle enters the electromagnetic calorimeter. This detector is composed of lead tungstate crystal blocks which measure the energy and position of electrons and photons striking it. While we have been describing a charged particle, a photon produced in the collision will, if not converted in the material of the upstream elements of the detector, travel in a straight line until it strikes the calorimeter. The calorimeter provides the only information we have about the photon. For electrons and photons, nearly all the energy of the particle is absorbed in the calorimeter. Muons will traverse the entire calorimeter losing only a little energy through ionization. Charged hadrons may begin to shower in the calorimeter or may pass through it losing energy only through ionization. Even if a hadron showers, the energy deposition will typically be only a fraction of the total energy.

The last detector in the system is the muon detector. This consists of two sections of

steel toroids, interspersed and followed by stations of proportional tube arrays. Hadrons escaping the calorimeter are absorbed in the first steel toroid. Muons traverse the toroid steel, bending in the field, and their momenta and angles are measured with the proportional tubes. Muons eventually enter the earth berm outside C0 where they loss all their energy.

The BTeV trigger is based on the property that most distinguishes all events containing $b$-flavored hadrons from events involving only light quarks: decay vertices separated from the primary vertex by distances consistent with lifetimes of $\approx$1.5 ps. We use this in the lowest level trigger, which we call Level 1, to select an eclectic mix of $b$ decays. This eliminates the need to use characteristics of specific final states which bias the experiment's sensitivity. To accomplish this, we must find both primary and secondary vertices at the lowest level of the trigger for every beam crossing of the Tevatron. These occur at a rate of 7.5 million per second. To do such sophisticated computations at such a high rate requires a massively parallel system of several thousand computational elements: Field Programmable Gate Arrays (FPGAs), Digital Signal Processors (DSPs), and microprocessors. While the Level 1 decision is being made, sparsified data for each crossing is stored in a large, multi-terabyte buffer memory made from commodity parts. There is no fixed latency for the Level 1 trigger. Whenever a decision is reached for a given beam crossing, data are either (effectively) deleted from the memory or (effectively) transferred to another memory to await subsequent processing. The events selected by the Level 1 trigger are further refined by the Level 2/3 trigger which is implemented with a system of several thousand conventional LINUX processors.

The data acquisition system includes the buffer memory system and the data highways over which events flow between the experiment front ends, the buffer memories, and the trigger processing elements. It also includes facilities to move data to large output disk buffers and eventually to record them on permanent media. It must also supervise the data flow, and control, monitor, and facilitate the troubleshooting of the entire system. It contains the "slow control system," which initializes and changes the parameters of the front-end systems. It also records non-event data, such as temperatures and pressures, provides the operator interface to the experiment, and maintains logs of all problems. It includes many databases required to support all these activities.

## 4.2 The C0 Experimental Area

The experiment will be carried out in the newly constructed C0 collision hall, shown in Figure 4.2. The hall is a 216 $m^2$ (9 m wide by 24 m long) enclosure centered on the C0 straight section of the Tevatron. The Tevatron beam is 2.5 m above the floor slab and 4.25 m below the roof of the hall. The enclosure specifications and dimensions are compatible with the detector described in this document.

To the east of the collision hall is the C0 assembly building, a steel framed, industrial type structure containing a 150 $m^2$ assembly hall at the collision hall elevation. The final assembly of detector components will occur in the assembly hall. They will then be moved into the collision hall through the 6 m $\times$ 6 m "shield door" opening. Figure 4.3 shows a

layout of the assembly building and collision hall with the vertex magnet and the muon toroids of the proposed BTeV detector superimposed.

Detector elements are brought into the area at a ground level loading dock and lowered to the assembly floor using the 30 ton crane which covers the loading dock and assembly hall. A large movable shielding wall separates the assembly area from the experiment enclosure. There are cable ducts from the experiment enclosure to a 150 $m^2$ equipment room at grade level on the north end of the assembly building. There will be a three level electronics/counting room and office area for experimenters.

## 4.3 BTeV Analysis Magnet

The vertex magnet in the proposed BTeV spectrometer is based on an existing magnet, the SM3 magnet, which is currently part of the decommissioned Fermilab MEast Spectrometer. It is shown, after modification, on the proposed layout, Figure 4.1, of the BTeV/C0 spectrometer. The magnet operated in MEast from 1982 until 1997, at a central field of about 0.8 Tesla, serving experiments E605, E772, E789, and E866.

The SM3 magnet was assembled by welding together, in place, various blocks of iron recovered from the Nevis Cyclotron. It has a total weight of 500 metric tons. After transportation to C0, the modified magnet will be reassembled in the C0 assembly hall and rolled into the C0 collision hall, as shown in Figure 4.3.

Studies with the magnetostatic modeling programs POISSON and OPERA have led to a design for a new pole-piece for SM3. This pole-piece, indicated in Figure 4.4, yields a central field of 1.5 Tesla, and an integrated dipole field of 5.0 T-m. The magnet will be oriented so that charged particles are deflected in the vertical plane. The properties of the magnet, with the pole faces shimmed to the BTeV requirements, are listed in Table 4.1. The vertical deflection of the Tevatron beam by the vertex magnet is compensated by two conventional dipoles at each end of the spectrometer.

Table 4.1: BTeV/C0 Vertex Dipole Properties

| Property | Value | Comment |
|---|---|---|
| $\int B \times dl$ | 5.0 T-m | 2.5 T-m on each side of center of IR |
| Central Field | 1.5 Tesla | |
| Steel Length | 3.2 m | |
| Overall length | 5.3 m | |
| Magnet Vert. aperture | $\pm$0.3 rad | |
| Magnet Horz. aperture | $\pm$0.3 rad | |

The magnet is centered on the interaction region thus creating the potential for two forward spectrometers. In quark-antiquark production at 1.8 TeV, the quark and antiquark

are usually either both boosted in the proton beam direction, or both boosted in the antiproton beam direction. Thus, having two spectrometers would double the acceptance of the experiment for tagged decays. Nevertheless, we initially plan to construct a single arm spectrometer only. Note that the second uninstrumented side can be used to test new detector concepts or prototypes of production components under actual beam conditions until it becomes possible to instrument the second arm.

In this central dipole geometry, there is a strong magnetic field at the vertex detector. Because of the excellent spatial resolution of the vertex detector, it is possible to get a crude measurement of the track momentum using the vertex detector alone, as outlined in the Pixel Detector section below.

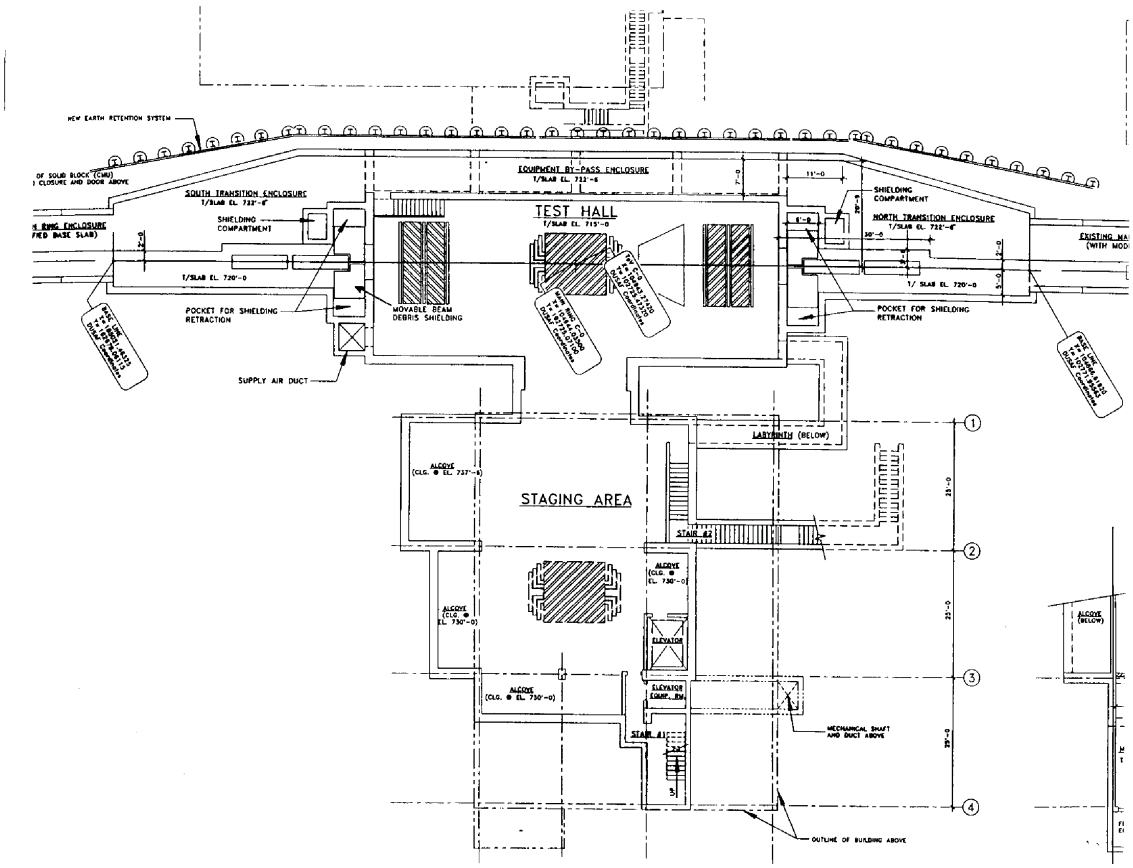


Figure 4.3: Layout of C0 Collision Area

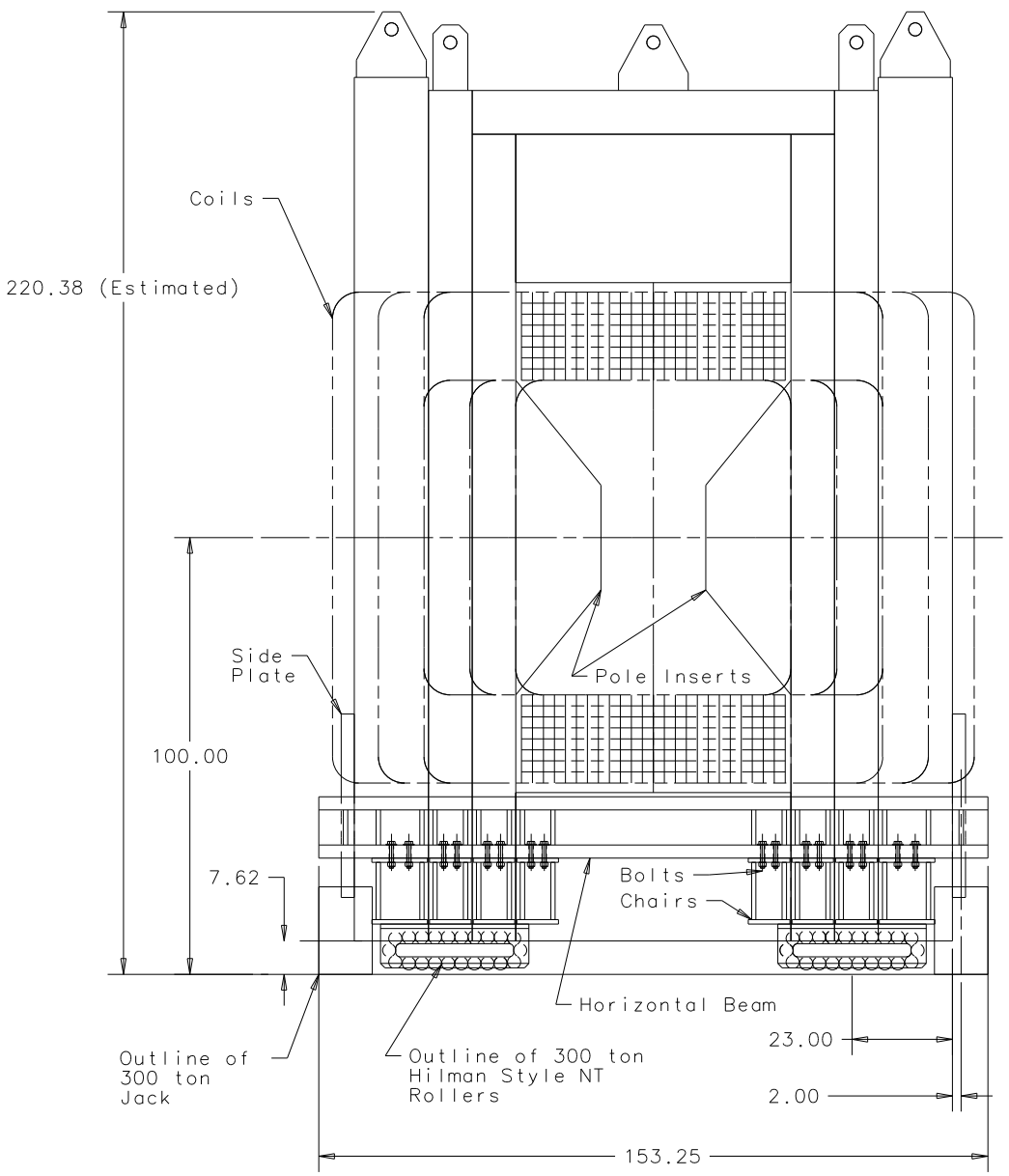


Figure 4.4: Cross section of the modified SM3 dipole with rollers and pole piece inserts. All dimensions are in inches.

## 4.4 Pixel Vertex Detector

### 4.4.1 Introduction

The vertex detector is critical to the success of BTeV. The key goals of the detector are excellent spatial resolution, ease of tracking pattern recognition, radiation hardness, material thinness, and readout of data fast enough for use in the lowest-level BTeV trigger system. The detector design has been guided by these goals, as will be described in the sections below. (This section is organized around these goals.) Many test results and details mentioned breifly here, are described in more detail in the R&D chapter.

### 4.4.2 Overview of Vertex Detector

The baseline vertex detector consists of a regular array of 30 "stations" of "planar" silicon pixel detectors distributed along the interaction region (Fig. 4.5). Each station contains one plane with the narrow pixel dimension vertical, and one with the narrow dimension horizontal. The stations are split, having a top half and a bottom half. Each half-station contains one (approximately) 5 cm $\times$ 10 cm precision vertical-position-measuring half-plane, and a smaller, (approximately) 3.8 cm $\times$ 7.3 cm horizontal-position-measuring half-plane. The top half-stations are positioned at regular intervals along the beam, and the bottom halves are similarly positioned, but midway between the top stations. This allows for possible overlap of half-planes with a variable-sized, small hole left for the beams to pass through. Table 4.2 summarizes the properties of the pixel detector.

The vertex detector contains nearly twenty-two million rectangular pixels, each 50 $\mu$m $\times$ 400 $\mu$m. Each sensor pixel is read out by a dedicated electronics cell. The sensor pixel and the readout cell are connected by a "bump bond." The basic building block of the detector is a hybrid assembly consisting of a sensor, a number of readout chips, and a flexible printed circuit (a high-density interconnect, HDI) which carries I/O signals and power. The sensors are variously sized to accept variable numbers of readout chips to make the required half-plane shape. Each readout chip is "flip-chip" mated to 22 columns of 128 rows of pixels on the sensors, corresponding to 2,816 active channels per readout chip. Each readout chip covers an active area approximately 0.64 cm $\times$ 0.92 cm. To avoid any dead space between adjoining read out chips, the pixels on the sensors corresponding to the edge of the readout chip (first and last column) are extended to 600 $\mu$m. These hybrid assemblies are supported by a movable carbon substrate that allows the pixel sensors to be positioned a safe distance away from the beam-line until stable conditions have been established in the Tevatron, at which point they are moved as close to the beam-line as radiation damage considerations will allow. This substrate also provides cooling for the readout electronics.

Fig. 4.6 shows a conceptual design for the aluminum vacuum vessel and carbon support structure for the pixel detector. The vessel is a rectangular box with a length of $\sim$ 165 cm and a height of $\sim$ 83 cm. Particles within the 300 mrad acceptance of the spectrometer traverse only the pixel stations and the 0.75 mm thick exit window. The carbon substrate

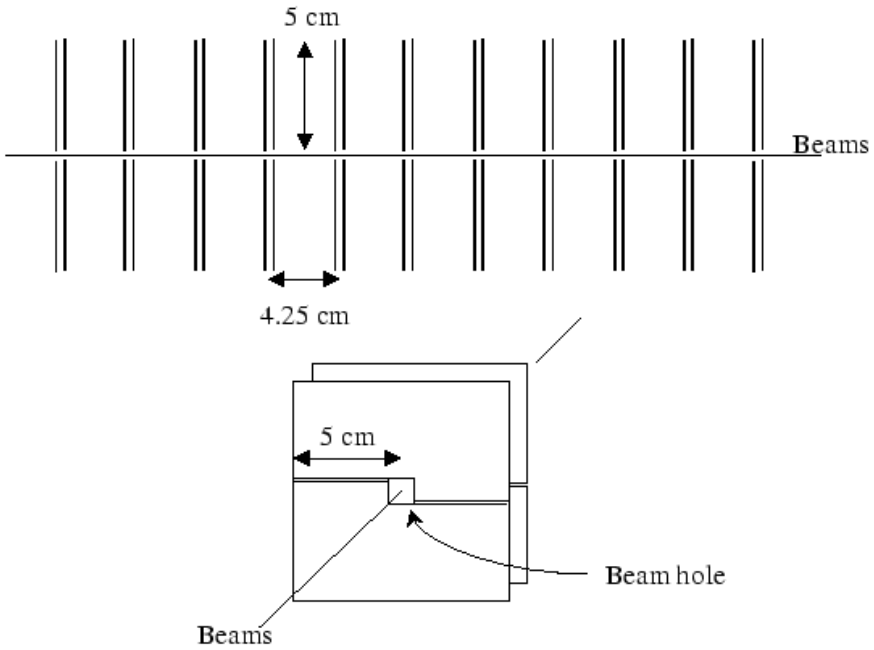


Figure 4.5: Schematic drawing of part of the pixel detector.

will be attached to a support frame made out of carbon fibers. Its position will be controlled by motors located just outside the vacuum vessel.

### 4.4.3 Spatial Resolution

BTeV test beam studies, performed with prototype sensors and readout having pixel sizes of 50 $\mu$m by 400 $\mu$m, have demonstrated a spatial resolution between 5 and 9 $\mu$m in the narrow dimension, depending on the track angle of incidence (see Fig. 4.7). The solid line shows the resolution function (Gaussian) used for the Monte Carlo studies presented in the BTeV proposal. The figure shows both the resolution obtained using 8-bit charge information directly, and also the resolution obtained by degrading the pulse height to 2-bits of information. This result confirms the prediction of our simulations:that excellent resolution can be obtained using charge sharing, even with very coarse digitization. Based on these results it has been decided that the BTeV readout chip will have a 3-bit FADC in each pixel cell. This will provide excellent spatial resolution. In addition, the actual pulse heights may be used to indicate the presence of $\delta$-rays or $\gamma$ conversions.

The single hit resolution is made possible by the choice of pixel size and a relatively low threshold for readout (approximately 2500 input electrons equivalent compared to about 24000 electrons for a minimum ionizing track at normal incidence for the devices tested).

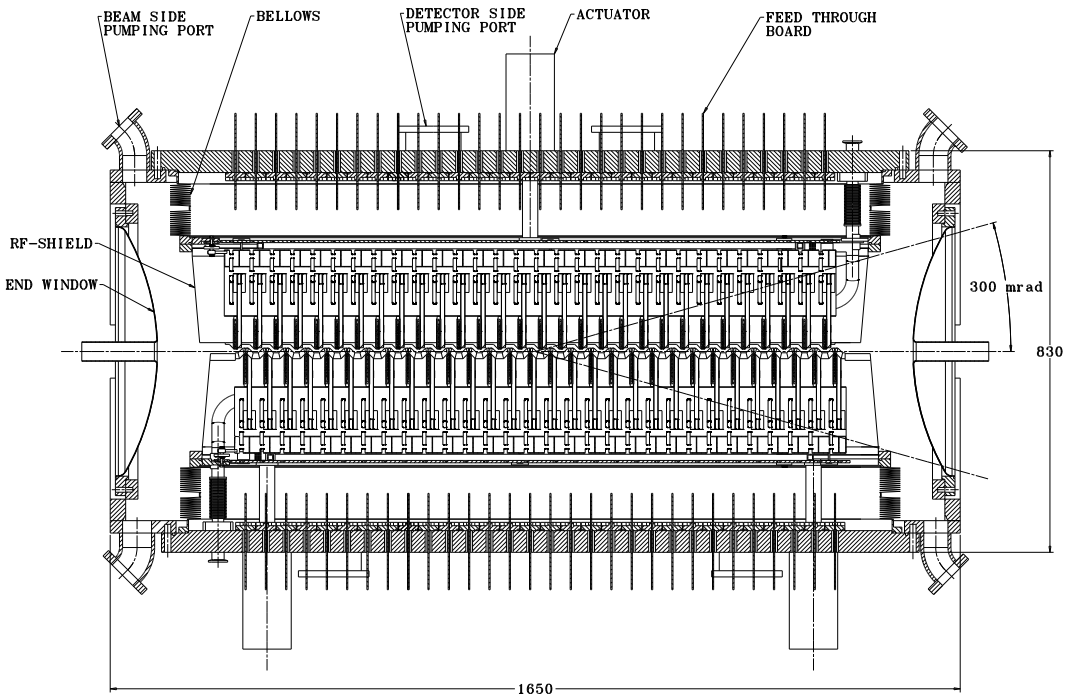


Figure 4.6: Side view of the vacuum vessel and support structure for the pixel detector. The pixel stations are mounted in two halves. Each half sits in a vacuum enclosure separated from the beam by a thin rf shield. Signals are fed through the vacuum vessel via printed circuit boards with high density connectors. Also shown in the figure are actuators and a bellows structure to allow the detectors to be moved in and out of the beam during data-taking and beam refill.

Relatively low dispersion of the thresholds across the chip and low noise in each pixel make the low readout threshold possible. Given the 132 ns beam crossing interval of the Tevatron, time slewing in the chips will not be a problem. While the above performance is for unirradiated devices, we anticipate operation at about -5 °C to minimize effects of radiation damage during the lifetime of the detectors. Mounting stability and the necessary pixel alignment, using actual tracks in the final location, will be important to avoid serious degradation of this good resolution.

While single hit resolution is important, it is not the whole story. We have worked to minimize the multiple scattering due to the material in all the components of the system. In addition to making the components of the detector proper as thin as possible (see Table 4.2), we allow only a thin membrane between the pixel detector and the beams. Thus, the pixel detector will sit in a secondary vacuum with only a thin aluminum rf shield between that vacuum and the accelerator vacuum. The very close proximity to the interaction region and the spacing between pixel planes is kept to a minimum to reduce the extrapolation distances to vertices, both primary and secondary. All these parameters have been optimized using

Table 4.2: Pixel Vertex Detector Properties

| Property | Value |
|---|---|
| Pixel size | rectangular: 50 $\mu$m $\times$ 400 $\mu$m |
| Outer Plane Dimensions | 10 cm $\times$ 10 cm |
| Central Square Hole (adjustable) | nominal setting: 12 mm $\times$12 mm |
| Total Planes | 60 |
| Total Stations | 30 |
| Pixel Orientations (per station) | one with narrow pixel dimension vertical & the other with narrow dimension horizontal |
| Separation of Stations | 4.25 cm |
| Sensor Thickness | 250 $\mu$m |
| Readout Chip Thickness | 200 $\mu$m |
| Total Station Radiation Length (incl. rf shielding) | 2.5% |
| Total Pixels | $2.2 \times 10^7$ |
| Total Silicon Area | $\approx$0. 6m$^2$ |
| Readout | analog (almost 3 bits, i.e., 7 thresholds) |
| Trigger | Signals are used in Level I trigger. |
| Rate Requirements | Time between beam crossings is 132 ns. |
| Noise Requirement | desired: $< 10^{-6}$ per channel/crossing required: $< 10^{-5}$ per channel/crossing |
| Resolution | better than 9$\mu$m |
| Radiation Tolerance | $> 6 \times 10^{14}$ particles/cm$^2$ |
| Power per Pixel | $\sim$60 $\mu$Watt |
| Operating Temperature | $\sim$-5 °C |

detailed (MCFast and GEANT) simulations of our experiment and representative physics measurements.

### 4.4.4 Pattern Recognition Capability

The early choice of pixel technology for the BTeV vertex detector was based, in part, on the space point information that it provides which will help in pattern recognition. Fig. 4.8 comes from a beam test of BTeV prototype pixel detectors, and shows the power of space points in reconstructing high density tracks. There, an interaction in a carbon target a few mm upstream of the first pixel plane leads to seven tracks reconstructed in much less than 1 cm$^2$, a density an order of magnitude more than typical for BTeV.

The pattern recognition capability benefits enormously from the low occupancy, averaging slightly above 1 track per $B$ event in the highest rate readout chip. In addition, the stretching

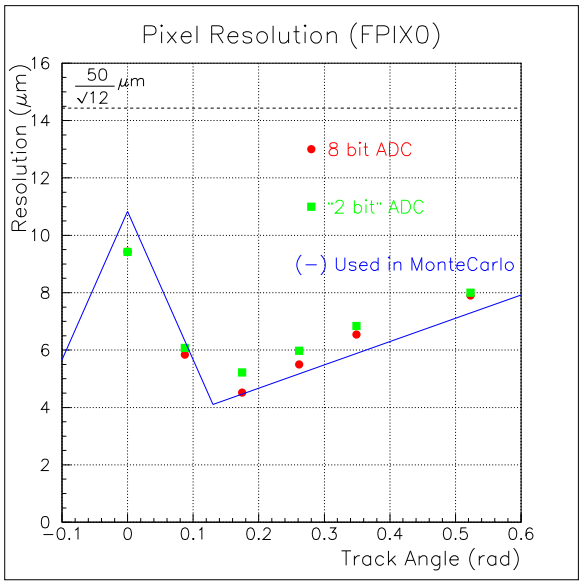


Figure 4.7: Resolution as a function of the angle of the incident beam for both 2-bit and 8-bit ADC readouts. The lines are piecewise linear fits to a simulation of the resolution.

of edge pixels and the shingled mounting (like the lapped wooden siding on a house) of the multichip pixel modules provide complete coverage within the nominal plane acceptance. The regular spacing of planes along the beam also eases the job of the Level 1 trigger.

### 4.4.5 Radiation Hardness

Solid-state device technology developments since the start of our BTeV efforts have eased concerns substantially in the area of radiation hardness. Our silicon sensors are based on n+/n/p technology as developed by LHC experiments. Our latest readout chips are manufactured with deep sub-micron (0.25 $\mu$m) CMOS technology, an inherently radiation-tolerant process, once enclosed-geometry transistors and appropriate guard ring designs are used. No redesign for military radiation-hard technologies, as planned in the past, is required.

Our tests have been made with irradiations up to $0.4 \times 10^{15}$ 200 MeV protons per cm$^2$ equivalent for our sensors (about 20 MRad) and $0.74 \times 10^{15}$ 200 MeV protons per cm$^2$ (equivalent to 43 MRad) for our readout chips. These tests show acceptable operation of sensors based on current and capacitance curves vs applied bias voltage, in terms of leakage current, required depletion voltage, and breakdown voltage. The readout chips in deep sub-micron technology appear to be even more radiation-hard. Radiation damage does not seriously affect noise, threshold dispersion, etc. up to these irradiation levels. These irradiation results will be augmented with charge collection and other tests in a Meson120 beam as soon as it is available this year. In addition, the measured rates of single event upset are low enough to be handled easily. No evidence of more serious single event effects has been seen. In addition, the plan is to operate the pixel detector at about -5 °C. This will

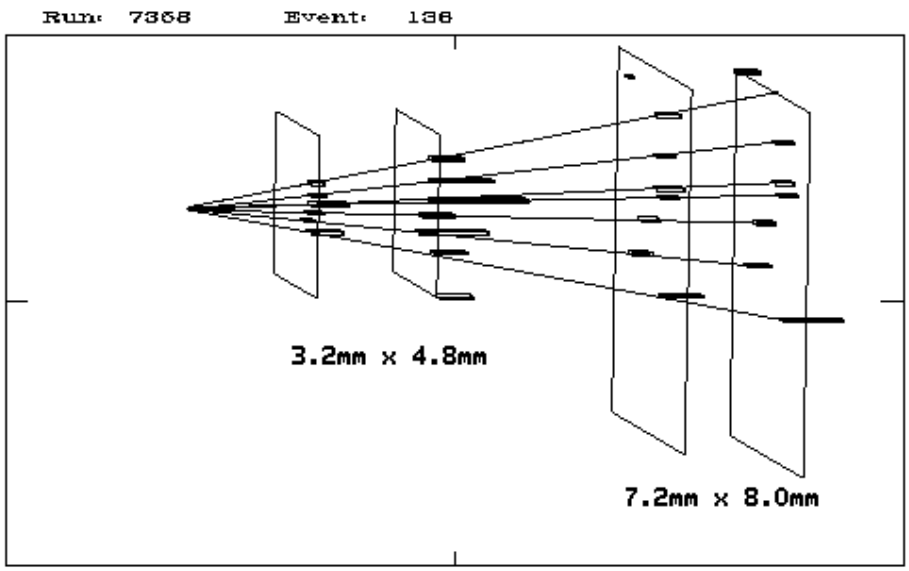


Figure 4.8: Multiparticle interaction observed in Fermilab beam test. The length of each hit is proportional to the pulse height. The straight lines represent fits to the outgoing tracks.

mitigate problems with charge trapping and reverse annealing (the variation in depletion voltage with time).

Finally, we will be testing all components (high density interconnects, adhesives, etc.) in high radiation environments before certification for use in the final detector.

### 4.4.6 Material Thinness

In order to prevent multiple scattering from decreasing the utility of our precision spatial resolution, we are keeping the material budget as low as possible. Table 4.3 lists the various contributions to our material budget. Note that the sensors and readout chips are thinned relative to what is typically used in high-energy physics today. The high-density interconnects and attached cables are minimal, with decoupling of signal and power cables so that the materials in each can be separately optimized. Both horizontal and vertical measuring half-planes share a single support substrate. The cooling is incorporated into this substrate, its design based on a system of glassy-carbon cooling tubes covered in highly thermally conductive "fuzzy carbon" to transmit heat to the water/glycol cooling fluid. This proprietary technology is required to reach the level of support material listed in Table 4.3. Given the risk in this approach, we are also working on fall-back solutions as described in the R&D chapter.

Table 4.3: Material budget of a BTeV pixel plane. The "Coverage" column shows the factors applied to account for overlaps of the sensors and readout chips, and for geometric coverage (e.g. area covered by bump bonds/total area); substrate coverage is listed as 0.50, because one substrate is shared by two planes. The numbers given for components on the HDI and for adhesive are derived from the ATLAS Pixel Detector TDR [1].

| *Item* | *Thickness(mm)* | $X_0(mm)$ | *Coverage* | $X/X_0(\%)$ |
|---|---|---|---|---|
| *Sensor* | 0.25 | 93.6 | 1.46 | 0.39 |
| *Readout chip* | 0.20 | 93.6 | 1.47 | 0.31 |
| *Bumps and wire bond* | 0.02 | 10.0 | 0.02 | 0.004 |
| *HDI* | 0.224 | 284 | 1.00 | 0.20 |
| *Components on HDI* | | | | 0.02 |
| *Adhesive* | | | | 0.02 |
| $Substrate(C-C)+coolant$ | 0.5 | 427 | 0.50 | 0.15 |
| $Shielding(Al)$ | 0.15 | 89.0 | 1.00 | 0.16 |
| *Total* | | | | 1.25 |

### 4.4.7 Readout Speed

Our pixel readout is data-driven. That is, the readout occurs as soon as data is ready on the readout chip. The token passing from row to row, which is an important part of the potential readout speed, is very fast (0.125 ns per row), and this starts in parallel in all columns. The readout rate allows us to move all the data off chip with negligible loss of data, even if the amount of data is three times that projected for our nominal luminosity of $2 \times 10^{32}$ cm$^{-2}$s$^{-1}$. Data output is serialized, but uses a number of parallel readout paths selectable for each readout chip. The bandwidth of each serial path is 140 Mbps. The chips located closest to the beam are each read out using 6 serial paths (840 Mbps total). Other chips are read out using 1, 2, or 4 serial paths. Most of the readout chips in the pixel system require only 1 serial output path. The readout bandwidth summed over the entire pixel detector is approximately 2 Tbps (terabits per second). The data coming off the chip is already highly sparsified, since only pixels above threshold are read out. Sorting out the data and assembling events is done external to the detector in large buffer memories.

### 4.4.8 Physics Capability

Figure 4.9 shows the distribution of $L/\sigma(L)$, which is the normalized detachment between the primary vertex and the $B$ decay vertex, for reconstructed decays $B_s \to D_s^- K^+$, where, $D_s^- \to \phi\pi^-$ and $\phi \to K^+K^-$. The mean value is 44 standard deviations! Figure 4.10 shows the L-resolution and the proper time resolution for the $B_s$ decay. The resolution in proper time is 46 fs even for this complex multibody decay containing a tertiary vertex (the $D_s^-$

decay). This can be compared with the $B_s$ lifetime of ∼1500 fs or the $B_s$ mixing period of ∼400 fs if $x_s$ is about 25. It is clear that the BTeV vertex detector has abundant resolution to carry out detailed time-dependent analyses even if the $B_s$ were to have a surprisingly high oscillation frequency.

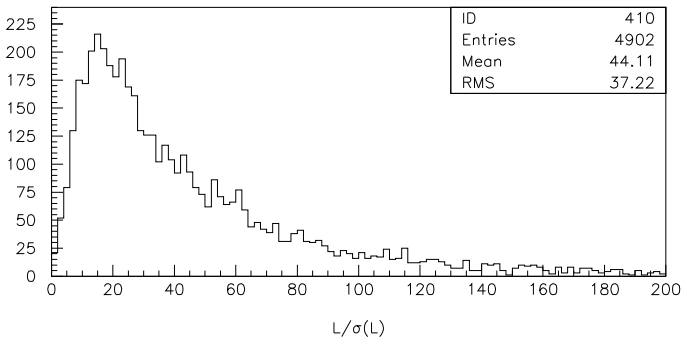


Figure 4.9: Normalized detachment, L/$\sigma$(L), between the primary vertex and the decay vertex for the decay $B_s \to D_s^- K^+$.

### 4.4.9 Summary

Over the last four years, BTeV collaborators have been working vigorously to establish a pixel detector capability for Fermilab, tuned to the unique features of the Tevatron crossing time and BTeV trigger needs. Since the earliest concerns were related to sensors, readout, and bump bonding, the primary focus has been on those issues. Progress has been gratifyingly rapid. This progress is evident in the success of the test beam effort at Fermilab, the results of which validate the ideas used for the BTeV proposal. The proposal to use a "shingled" fuzzy carbon support and cooling structure is undergoing mechanical and cooling capacity tests, as is a beryllium alternative.

Yields of all pixel-related components have been high enough that thus far we have made working prototypes without major production duplications. Thus, we may hope that our focus on simplicity within our aggressive technical approach will succeed. This approach, combined with the early implementation of a significant subsample (∼10%) of final-design detectors, should allow reliable planning and achievment of the goals of the experiment.

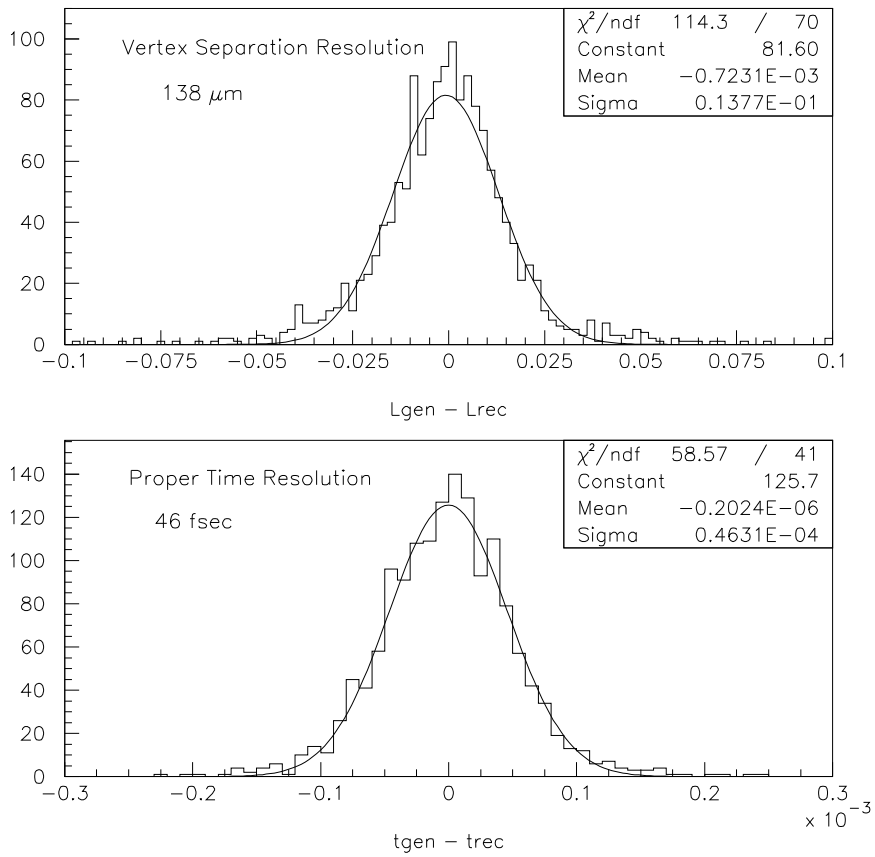


Figure 4.10: Top) The resolution in L, the separation between the primary and secondary vertex. The quantity plotted is the difference between the Monte Carlo generated separation $L_{gen}$ and the reconstructed separation $L_{rec}$, for the $B_s$ decay. The X- axis is in cm. The L resolution is 138 $\mu$m; and bottom) the resolution in proper time. The quantity plotted is the Monte Carlo generated proper time $t_{gen}$ minus the reconstructed proper time, $t_{rec}$ of the $B_s$ decay. The X-axis is picoseconds ($10^{-3}$ nanoseconds). The proper time resolution is 46 fs.

## 4.5 Forward Tracking System

### 4.5.1 Introduction

The major functions of the forward charged particle tracking system are to provide high precision momentum measurements for tracks found in the pixel system, to reconstruct and measure all parameters for tracks which do not pass through the vertex detector (such as $K_s$ and $\Lambda^o$ daughter tracks), and to project tracks into the RICH counters, EM calorimeters, and Muon detectors. Measurements from the forward tracking system are also used online in the Level 3 trigger, as explained below.

#### 4.5.1.1 General Description

The baseline forward tracking system consists of 7 stations in one arm, placed transversely to the beam at various distances from the interaction point. Three stations are placed inside the dipole magnet, three stations in the low field region just upstream of the RICH, and one station just downstream of the RICH. The entire system extends over a distance of $\sim$7 m and provides polar angle coverage from approximately 10 mr up to 300 mr.

The design of the forward tracking system has been driven by the high density of tracks produced in the forward direction, especially with multiple interactions per crossing. Two different types of detectors are used. Most of the solid angle is instrumented using straw tube drift chambers. Straws have been chosen because they can be used to make large chambers with small cell size, and because they are immune to catastrophic failure of an entire detector from a single wire break. The track density very close to the beam requires detectors with even higher granularity; we have chosen to instrument the central section of each station with silicon microstrip detectors.

Tables 4.4 and 4.5 list all the geometric parameters and the main characteristics of the forward tracker. This forward tracking system configuration has sufficient segmentation to handle the high hit multiplicities that are expected when $b\overline{b}$ events are produced in the forward region along with minimum bias events. Fig. 4.11 shows occupancies in the straw tracker predicted by BTeVGeant for the case in which a $b\overline{b}$ event is produced at the design luminosity of $2\times10^{32}$ cm$^{-2}$ s$^{-1}$. The maximum occupancy is 4% in the silicon strip detectors, which have 40 times finer pitch than the straw chambers.

#### 4.5.1.2 Forward Tracker Performance

The system just described ensures excellent tracking performance over the full acceptance of the forward spectrometer. Figure 4.12 show the expected average fractional momentum resolution for $b$ decay products as a function of track momentum and of the track production angle with respect to the beam axis. For these histograms, an effective position resolution of $\sigma_{X,U,V} = 150$ $\mu$m was assumed for each view of the straws and a resolution of $\sigma_{X,U,V} = 29$ $\mu$m assumed for the silicon strip detectors.

Table 4.4: Properties of the baseline forward straw tracker (1 arm)

| Property | Value |
|---|---|
| Straw size | 4 mm diameter |
| Central hole | 27 cm × 27 cm |
| Total Stations | 7 |
| Z positions (cm) | 95, 138, 196, 288, 332, 382, 725 |
| Half size (cm) | 27, 41, 61, 88, 102, 116, 204 |
| Views per station | 3 (X,U,V) |
| Layers per view | 3 |
| Total number of straws | 29,088 |
| Total station thickness | 0.6% $X_0$ |
| Total channels | 58,176 |
| Readout | ASD + timing chip (6 bits), sparsified |

Table 4.5: Properties of the baseline forward silicon tracker (1 arm)

| Property | Value |
|---|---|
| Si-sensors | $\sim 7 \times 7$ cm$^2$, $p$-on-$n$ type |
| Pitch | 100 $\mu$m |
| Thickness | 200 $\mu$m |
| Sensor configuration | 4 ladders of 4 sensors |
| Coverage | 27cm × 27cm |
| Central hole | 5.4 cm × 5.4 cm (7 cm × 7 cm in last station) |
| Total stations | 7 |
| Z positions (cm) | 99, 142, 200, 292, 336, 386, 729 |
| Views per station | 3 (X, U, V) |
| Channels per view | ∼5,600 |
| Total channels | ∼127,600 |
| Readout | sparsified binary |

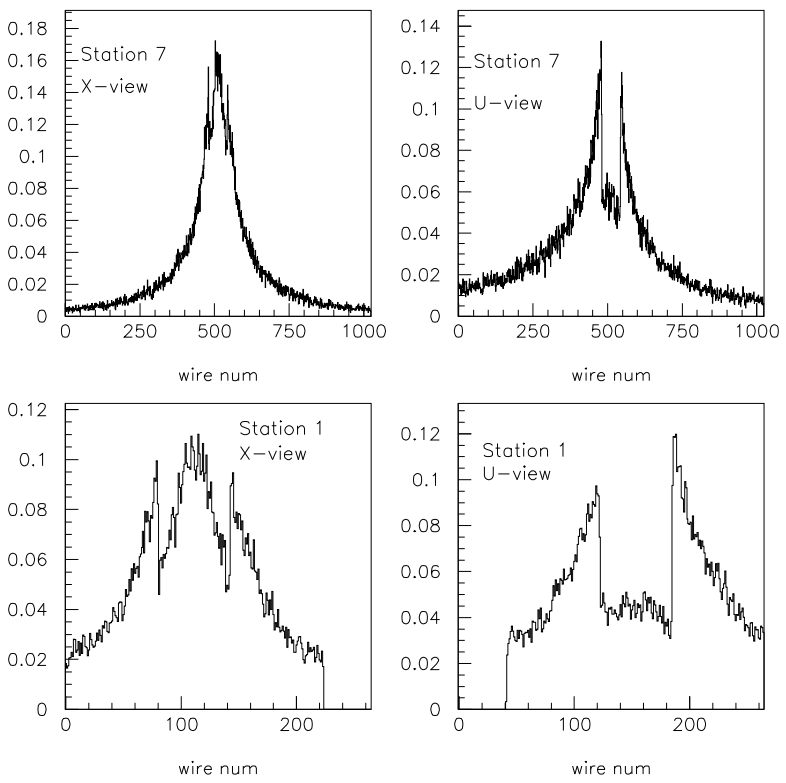


Figure 4.11: Occupancies in the first station of straws, Station 1, and the station just upstream of the EM Calorimeter, Station 7, when a $b\overline{b}$ event is produced at the design luminosity of 2 $\times 10^{32}$ cm$^{-2}$ s$^{-1}$. The two histograms on the left are for X-view straws, while those on the right are for U-view straws. The V-views have identical occupancies to the U-views.

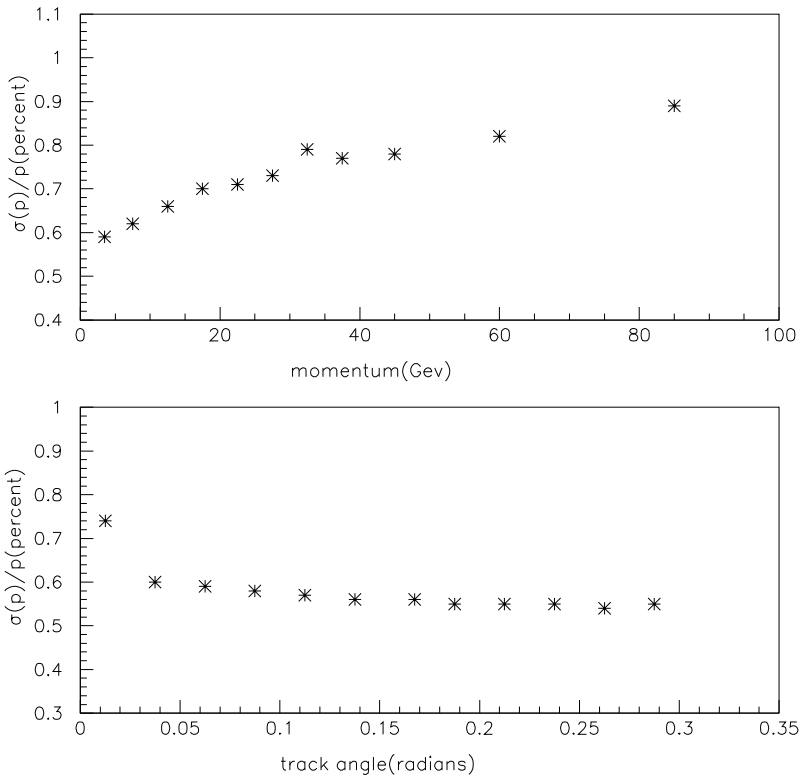


Figure 4.12: Momentum resolution as a function of track momentum (upper plot) and as a function of polar production angle (lower plot) for $b$ decay products.

### 4.5.2 Forward Silicon Tracker

#### 4.5.2.1 Detector Description and Layout

Our design consists of stations with three planes of 200 $\mu$m thick single-sided silicon microstrip detectors with 100 $\mu$m pitch. The silicon sensors, which have an area of $7 \times 7$ cm$^2$, are arranged in ladders of 4 daisy-chained sensors each in such a way that four adjacent ladders form a plane as illustrated in Fig. 4.13. The ladders are mounted on a low mass carbon fiber support which is designed to ensure a relative proper alignment among all the elements of the plane and also among different planes of the same station as described in the R&D section of this document.

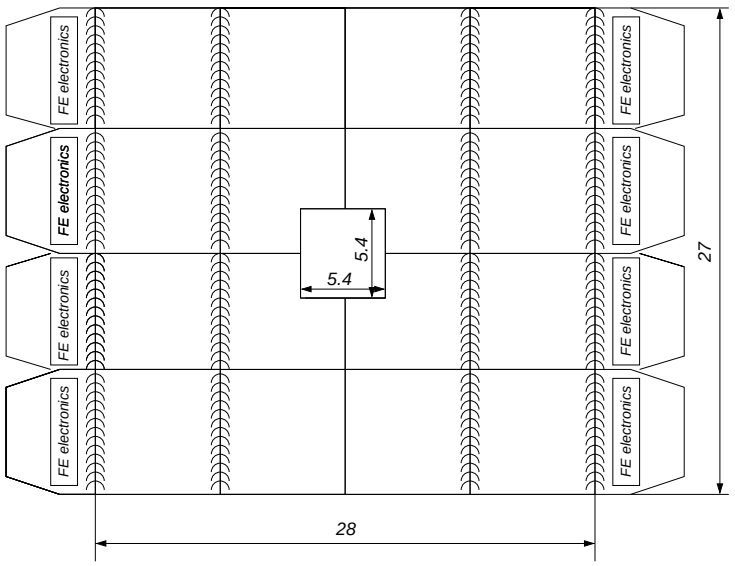


Figure 4.13: Sketch of a silicon detector plane. It consists of 4 ladders of four daisy-chained Si-sensors. The two pairs of sensors on each ladder are read-out separately by the front-end electronic chips placed at the two ends of the same ladder. There is some overlap between adjacent ladders to ensure good efficiency over the entire plane. Dimensions are in centimeters.

Three views, called $X$, $U$ and $V$, are provided by rotating two of the planes. The two stereo views, $U$ and $V$, are at $\pm$ 11.3$^o$ around the $Y$ bend coordinate. Each plane consists of about 5,600 readout channels; the entire system of 7 stations has about 128,000 channels in total (1 arm).

The Si-sensors are of the standard $p$-on-$n$ type, with multiple guard rings to allow high voltage operation. The front-end electronics is distributed along the two opposite edges of each plane where it is cooled by a fluid circulating in a duct embedded in the support structure around the periphery of the plane.

The preamplifier chips are AC coupled to the strips by means of capacitors directly

integrated on the sensors. Each channel is read out in binary mode providing a $\sigma$ = 100 $\mu$m/$\sqrt{12}$= 29 $\mu$m resolution, adequate for our physics goals.

We do not foresee any major problems in building these detectors since we can profit from the enormous experience accumulated in CDF and D0 at the Tevatron, as well as other experiments, and from the ongoing R&D programs for LHC.

#### 4.5.2.2 Radiation Issues

It is well known that the exposure of silicon detectors to high radiation doses causes damage that limits their useful lifetime. Thanks to the enormous progress accomplished during the last few years, we can now build detectors that can be operated after exposure to fluences in excess of $10^{14}$ particles/cm$^2$ [5].

In BTeV, we expect a radiation level at the silicon detectors that decreases rapidly with increasing distance from the beam. Important radiation damage effects, if any, will be confined to a small region closest to the beam line.

The highest levels of radiation occur at the station closest to the interaction region. As shown in Fig. 4.14, the maximum value of the fluence is expected to be $\sim 1.6 \times 10^{13}$ particles/cm$^2$/year, given a luminosity of 2 $\times 10^{32}$ cm$^{-2}$ s$^{-1}$. This is slightly less than the dose expected for Layer 0 of the CDF silicon tracker at the same luminosity [6]. With a proper choice of sensors, we will operate our detectors with a safety margin superior to that of CDF and those of LHC experiments. In the worst case scenario, we can expect serious radiation damage effects only on a minor portion of our detectors close to the beam after several years of operation.

#### 4.5.2.3 Readout Electronics

Even given the low occupancy expected in the Forward Silicon Tracker, the output bandwidth required to read out all hit information from every crossing is higher than is provided by any silicon strip detector (SSD) readout chip, either already fabricated or being developed for another experiment. For this reason we have decided to develop a new readout chip with very high readout bandwidth. We will also take the opportunity to design a continuous-time-filter preamplifier capable of exploiting all the advantages offered by the relatively long bunch-crossing period of the Tevatron collider (T = 132 ns). We are designing a new preamplifier which should feature an ENC $\sim$1000 $e^-$ for semi-Gaussian shaping with 100 ns peaking time and a capacitive load at the input of $\sim$20 pF, as expected for our longest strips. This noise performance represents in our view "the state of the art" for silicon strip preamplifiers.

The binary readout we are presently considering is a simplified version of the readout scheme implemented in the FPIX2 pixel readout chip. It is very fast and employs a flexible scheme for zero-suppression and readout, that can be easily adapted to strips. The SSD readout chips will be designed to interface to the same electronics we will employ to read out pixel chips.

The new read-out chip will be implemented using 0.25 $\mu$m CMOS technology, following the radiation tolerant design rules developed for the FPIX2 design.

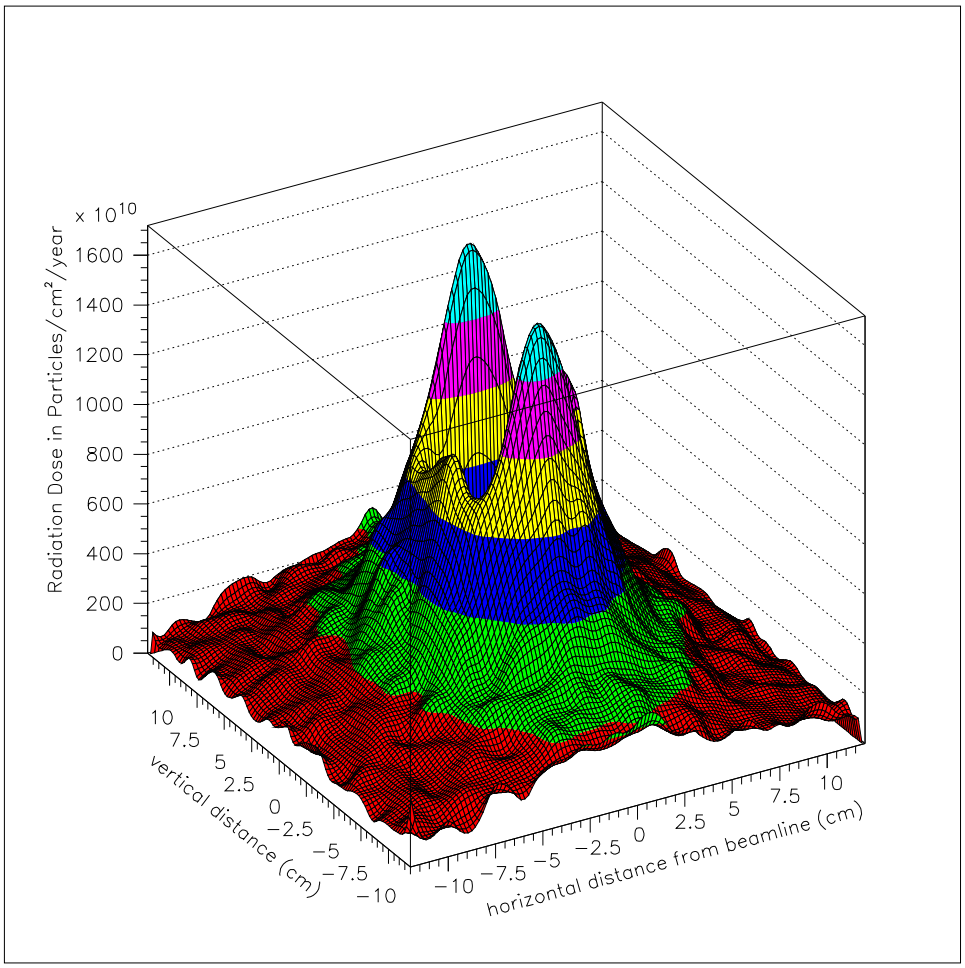


Figure 4.14: Radiation dose as a function of position in Forward Silicon Tracker Station # 1. The horizontal magnetic field concentrates more particles above and below the square central beam hole than on either side.

Figure 4.15: A photograph of one of the BTeV 3.97mm diameter × 8mm length twisters. The material is Ultem plastic. Of key importance is the smooth cut edges, which prevent the sense wire from snagging during the stringing process. The depth of the spiral groove is 2.00 mm, which nominally centers the 25 micron sense wire along the longitudinal axis of the twister.

### 4.5.3 Forward Straw Tracker

#### 4.5.3.1 Detector Description and Layout

The forward straw tube tracker consists of stations that provide 3 coordinate measurements, $X$, $U$ and $V$, where the two stereo views, $U$ and $V$, are at $\pm$ 11.3$^o$ around the $Y$ bend coordinate, same as in the forward silicon detector. With three layers per view, this configuration provides excellent resolution in the bend plane while maintaining a robust ability to reject ghost combinations of hits. It has sufficient redundancy to achieve a high detection efficiency and to resolve the left/right ambiguity a very large fraction of the time. The unit of construction is the "half-view", itself composed of a number of 48 straw modules. Two half-views fit around the beampipe to make up a single view.

All the sense wires for the straw cells that do not terminate at the central hole are divided electrically using a small glass capillary bead following the technique used for the ATLAS TRT [3]. This cuts the occupancy rates in half. In addition, within a 27 cm square region of the beam pipe, all straw sense wires are deadened by using two glass capillary beads to isolate the central section of the sense wire. This is done to lower the straw occupancy rates. This region is covered by the Silicon Strip tracker. The sense wires in straws that span more than 80 cm have additional supports (twisters), which are realized following the helical design developed for the SDC Straw Prototype. One of our twisters is shown in Fig. 4.15.

The smooth edges avoid any sense wire snags during the stringing process.

The time between bunch crossings in the Tevatron will be 132 ns by the time BTeV is operational. This time allows the use of standard gases like Argon-Ethane or Argon-$CO_2$, which have drift times in our 4mm straws on the order of 60 ns. We are undertaking an extensive R&D program on the aging properties of these and other gases.

#### 4.5.3.2 Front End Electronics and Drift Time Measurement

The straw tube chambers will be instrumented using electronics developed by the University of Pennsylvania [4], initially for the SDC straw chambers, the CDF Central Outer Tracker and more recently for the ATLAS TRT. These radiation hard integrated circuits include high gain preamplifiers, pole-zero networks for pulse shaping and ion-tail cancellation, and leading edge discriminators.

The drift time will be measured using digital TDC's. The information from the straw tracker, like all information from every subsystem in the BTeV spectrometer, must be digitized and read out for every crossing. This means that a new TDC must be designed for BTeV. The small diameter of the straws makes the specifications of this TDC easy to achieve. A six-bit single-hit TDC, with 1.5 ns wide bins covering 96 ns, is sufficient to provide a drift distance measurement precision better than 100 $\mu$m. It is worthwhile recalling that even without a TDC, we can locate the track in a particular view with an rms uncertainty of 600 $\mu$m.

#### 4.5.3.3 Technical issues

We are developing a prototype straw tube which places an aluminum conduction layer between two Kapton films, the inner one next to the gas volume being a carbon loaded, low resistivity film. The idea is that the Kapton forms a protective barrier, similar to the graphite layers deposited on the inner surface of the ATLAS TRT straws. Without this protective barrier, there is a danger that the aluminum layer may be etched away, limiting the lifetime of the straw. We measured the surface resistivity of the aluminum coated, carbon loaded Kapton film of our prototype to be $6.5 \pm 1.0$ $\Omega$/square, which is comparable to the specified value for the TRT straw tube. The details of the prototype straw material are listed in Table 4.6.

Currently we have built multiple single straw prototypes using this straw. We have measured gas gains and gain uniformity along the straw, with the straw straightness provided by tensioning the straw. A one meter, two-module (96 straws in total) prototype detector (Fig 4.16) is under construction. It will be tested in the Fermilab Test Beam this year.

| Description | BTeV Straw Prototype |
|---|---|
| Kapton film | Inner: Polyimide type XC<br>$25 \pm 2.5$ $\mu m$ thickness<br>Outer: Polyimide type 100 VN<br>$25 \pm 2.5$ $\mu m$ thickness |
| Density | 1.42 g/cm$^3$ |
| Aluminum layer | $(0.2 \pm 0.08) \mu m$ thickness |
| Resistivity of inner Kapton layer | $6.5 \pm 1.0$ $\Omega$/square |

Table 4.6: Summary of material specifications for the BTeV prototype straw tubes

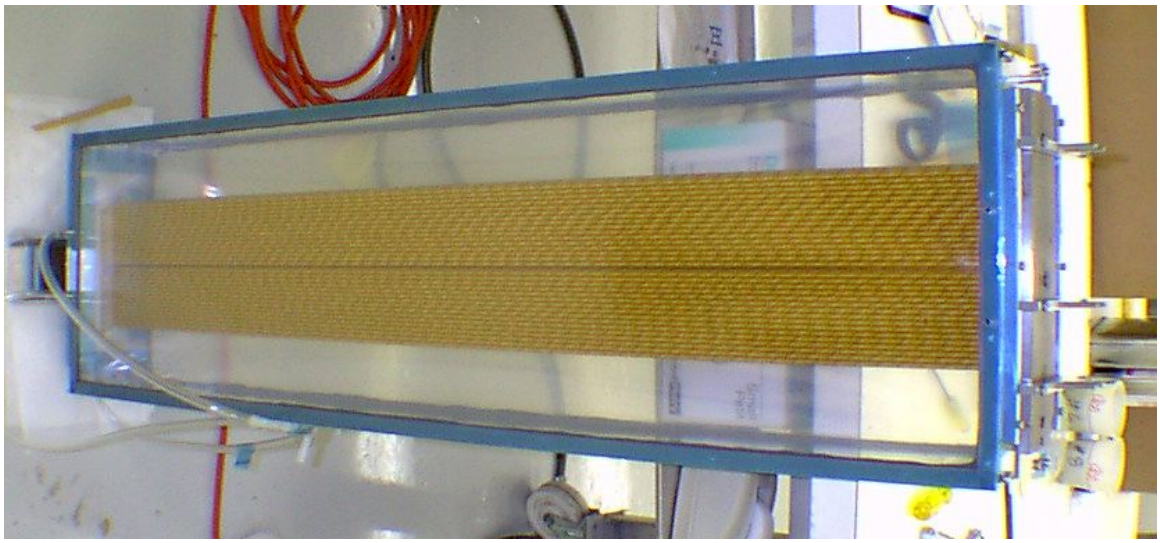

Figure 4.16: The BTeV Straw Prototype Detector (under construction) showing the modularity which is anticipated for the actual detector. Each module contains 48 straws, in three close-packed planes.

## 4.6 Charged Particle Identification

Excellent charged hadron particle identification is a critical component of a heavy quark experiment. Even for a spectrometer with the excellent mass resolution of BTeV, there are kinematic regions where signals from one final state will overlap those of another final state. For example, $B_s \to D_s K^-$ signal must be distinguished from $B_s \to D_s \pi^-$ background in order to measure the CKM phase $\gamma$. These ambiguities can be eliminated almost entirely by an effective particle identifier. In addition, many physics investigations involving neutral $B$-mesons require "tagging" of the flavor of the signal particle by examining the properties of the "away-side." Our studies show that kaon tagging is a very effective means of doing this. "Same-side" kaon tagging is also very effective for $B_s$ mesons.

### 4.6.1 Requirements

In the design of any particle identification system, the dominant consideration is the momentum range over which efficient separation of the various charged hadron types – $\pi$, $K$, and $p$ – must be provided. In BTeV, the physics goal which sets the upper end of the momentum requirement is the desire to cleanly separate $B_d^o \to \pi^+\pi^-$ from $B_d^o \to K^+\pi^-$ and $B_s^o \to K^+K^-$. These two-body decays produce reasonably high momentum pions and kaons. Fig. 4.17 shows the momentum distribution of pions from the decay $B_d^o \to \pi^+\pi^-$ for the case where the two particles are within the spectrometer's acceptance. The low momentum requirement is defined by having high efficiency for "tagging" kaons from generic $B$ decays. Since these kaons come mainly from daughter $D$-mesons in multibody final state $B$-decays, they typically have much lower momentum than the particles in two body decays. Fig. 4.18 shows the momentum distribution of tagging kaons for the case where the signal particles are within the geometric acceptance of the spectrometer. About 1/5 of the tagging kaons never exit the end of the spectrometer dipole. Almost all kaons exiting the dipole have momenta above 3 GeV. Based on these plots, we have set the momentum range requirement for the particle identification system to be

$$3\,\mathrm{GeV/c} \quad < \quad P_{particle\ id} \quad < \sim 70\,\mathrm{GeV/c} \tag{4.1}$$

Finally, kaons and pions from directly produced charm decays have momenta which are not very different from the kaons from $B$-decays. The range set by the $B$-physics requirements is a reasonable, if not optimal, choice also for charm physics.

### 4.6.2 RICH radiators

Because of the large particle momenta there is really only one choice of detector technology – a gaseous ring-imaging Cherenkov counter. Pions and kaons can be separated in the required momentum region with a single gas radiator. We choose $C_4F_{10}$ which has an index of refraction of 1.00138 in the visible range. The momentum dependence of the Cherenkov angle for pions, kaons and protons in this gas is shown in Fig. 4.19. Many other experiments

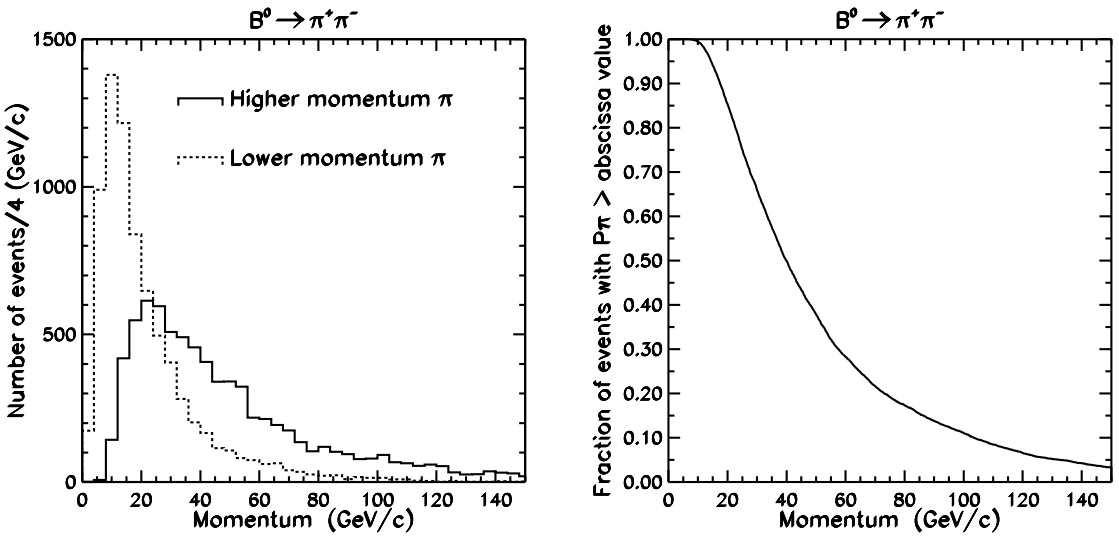


Figure 4.17: The momentum distribution of pions in $B_d \to \pi^+\pi^-$ decays. The left plot shows distributions for the lower (dashed line) and higher (solid line) momentum pion in this decay. The right plot presents the latter distribution in integral form, which gives loss of efficiency as a function of the high momentum cut-off of the particle ID device.

use this gas, including DELPHI (endcap) [7], HERA-B [8] and HERMES [9]. It was also chosen for one of the LHCb RICH detectors [10].

Note that below about 9 GeV, no gas can provide $K/p$ separation and that, since kaons are below threshold, the RICH operates in a threshold mode for ($K$ or p) vs. $\pi$ separation (except that it has much better noise discrimination than a normal threshold counter because it still measures a Cherenkov ring for pions). $K/p$ separation turns out to be important for $b$-flavor tagging. In the case of the $B_s^o$, we use a positively identified kaon for for both "same side" and "away-side" tagging. For the $B_d$, only the "away-side" case requires kaons. In the "same side" tag, there is a strong correlation between the sign of the fragmentation kaon and the flavor of the $B_s$. However, the tagging fragmentation kaon comes from the primary vertex which also contains many protons that can cause false tags. In "away-side" tagging, the lack of $K/p$ separation prevents one from distinguishing kaons from $p, \bar{p}$, which occur 8% of the time in $B$ meson decays and a much larger $\sim$50% for $\Lambda_b$ decays.

In the BTeV proposal, there was a plan to improve identification of low momentum particles by inserting a thin ($\sim$ 4cm) piece of aerogel at the entrance to the gas RICH as proposed by LHCb [11] and already implemented by HERMES [9]. The Cherenkov rings were focused by the mirrors of the RICH and fell on the same photon detector array (somewhat enlarged) as the Cherenkov photons emitted in the $C_4F_{10}$. A study using detailed reconstruction of the Cherenkov rings showed that the relatively low light yield of the aerogel, combined with confusion from the larger number of overlapping rings from higher momentum tracks radiating in the $C_4F_{10}$, resulted in very little particle discrimination.

Recently, a new plan has bean adopted in which the aerogel radiator is replaced by a

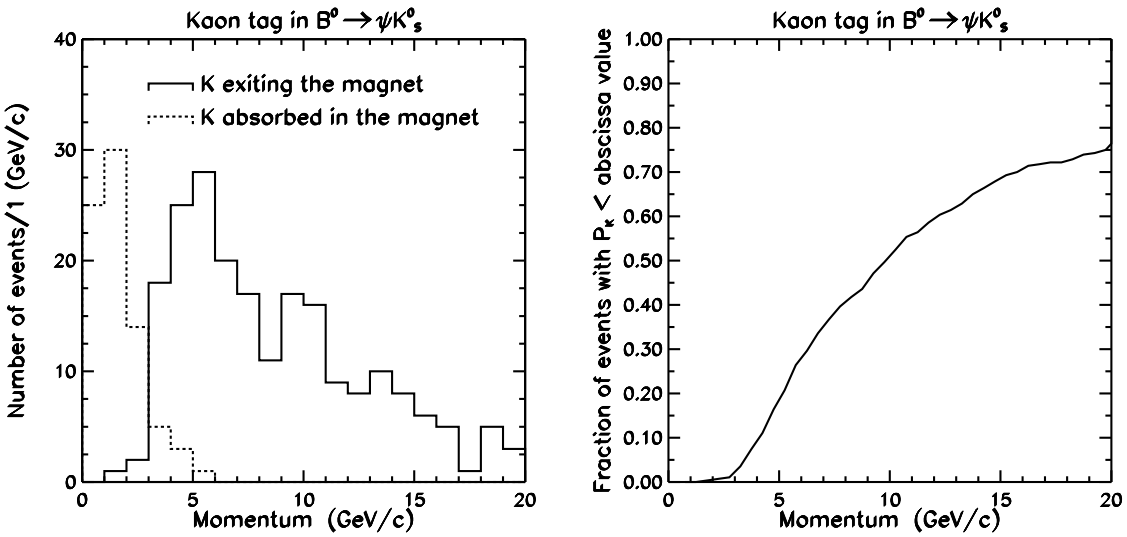


Figure 4.18: The momentum distribution of "tagging" kaons for the case where the signal particles ($\psi K^0_S$) are within the geometric acceptance of the spectrometer. The left plot shows distributions for kaons absorbed in (dashed line) and exiting from (solid line) the magnet. The right plot presents the latter distribution in integral form, which gives loss of efficiency as a function of the low momentum cut-off of the particle ID device.

liquid radiator. The selected liquid, $C_5F_{12}$, has an index of refraction of 1.24, compared to 1.03 of aerogel. This produces more intense Cherenkov rings even from a very thin layer of liquid. The rings are also larger so that 2/3 of the photons impinge on the side walls of the RICH gas containment vessel, which is covered with photomultipliers to record them. The Cherenkov photons radiated in the gas radiator ($C_4F_{10}$) are reflected and focused by the RICH mirror and almost never arrive at the side walls. Thus, the two main limitations of the aerogel scheme, the low amount of Cherenkov light and the confusion between Aerogel photons and $C_4F_{10}$ photons are eliminated. At the same time, the refractive index of $C_5F_{12}$ is low enough, that kaon and proton rings have very different radii, even at 9 GeV, and can be distinguished with relatively large diameter photomultiplier tubes (to keep the cost low). Although about 1/3 of the photons from the liquid radiator are focused by the RICH mirror, they are imaged outside the sensor planes which detect the $C_4F_{10}$ photons and thus cause no problem to the RICH pattern recognition.

### 4.6.3 RICH dimensions

The RICH detector can be located behind the tracking chambers just outside the central dipole magnet, about 4 meters away from the interaction point. The length of the RICH detector must be less than 3 meters to allow sufficient space for the EM calorimeter and the muon system.

The liquid radiator with thickness of about 1 cm will be mounted at the entrance to the

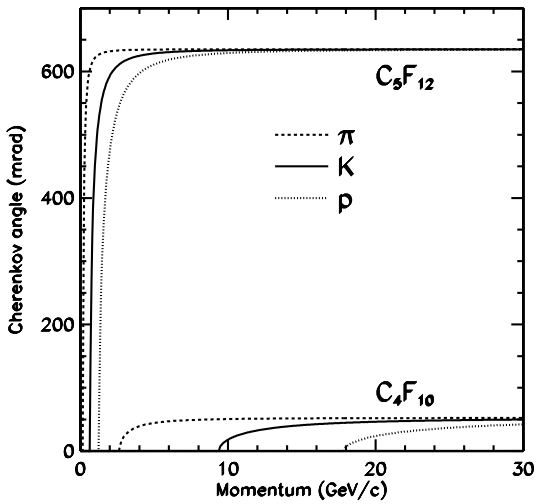


Figure 4.19: Cherenkov angles for various particle species as a function of particle momentum for $C_4F_{10}$ and liquid $C_5F_{12}$ ($n = 1.24$) radiators.

RICH vessel. It will cover the entire RICH entrance window, except for a rectangular square around the beam-pipe. The liquid is supported by a 3 mm thick carbon fiber backplane and a 3 mm thick quartz window (for radiation hardness).

Spherical mirrors at the end of the gas volume reflect Cherenkov photons, radiated in the $C_4F_{10}$ and focus them into rings at the photo-detection surface. The photo-detectors should be located away from the flux of particles exiting the magnet, therefore the mirrors are tilted. In order to minimize geometric aberrations from an off-axis mirror configuration, the mirrors will be split along the mid-line of the detector, reflecting photons to photo-detectors located on each side of the vessel in the non-bend view ($x - z$ plane). The longer the RICH detector the smaller the tilt angle. Since the geometric aberrations due to the mirror tilt are significant for the gas radiator, we plan on the longest RICH detector we can accommodate within the space limitations. This also maximizes the photon yield from the gaseous radiator, again improving the resolution of the device. Thus, the gas radiator will be approximately 3 meters long and the mirror radius will be 7 meters. The mirror tilt angle will be 261 mrad. Note that the mirror tilt angle cannot be further reduced by use of additional flat mirrors at the other end of the detector, as in the designs of HERA-B and downstream LHC-b RICH detectors, since the front of the gas volume must stay transparent to the $C_5F_{12}$ photons. (Such a scheme would be difficult even without the liquid radiator since there is not enough lateral space in the experimental hall.) The transverse size of the mirror will be about 4 m $\times$ 4 m. A possible configuration for the mirrors is to make them from an array of individual hexagons. Each mirror half would consist of 18 full hexagons (76.2 cm tip-to-tip) and 6 half hexagons. A reflectance efficiency of about 90% has been achieved in HERA-B detector with 7 mm thick Pyrex coated with 200 nm Al and 30 nm $MgF_2$. We are investigating lower mass mirror materials.

To find the size and optimal position and orientation of the photo-detection surface, we have used a ray tracing Monte Carlo. Even though the true focal plane of a spherical mirror is not planar, non-planar surfaces do not improve resolution significantly and are difficult to realize in practice. Thus, we have assumed that the Cherenkov rings are focused on a plane. Photo-detection systems considered (see the next section) work the best for normal light incidence. Thus the photo-detection plane must be tilted in the $x - z$ plane to follow the mirror tilt. Simulation indicates that a tilt by 442 mrad produces normal incidence on average. Since the actual emission point along the track for Cherenkov photon is unknown, the Cherenkov angle reconstruction assumes emission at the track mid-point. The emission point error contributing to Cherenkov angle resolution is magnified by mirror tilt from 0.2 mrad to 0.53 mrad. This error imposed by geometrical considerations sets the scale for the other two major contributions to Cherenkov angle resolution: chromatic error and photo-detector segmentation error (called also photon position error) which can be controlled by parameters of the photo-detection devices.

The photons generated in the liquid radiator pass through the quartz exit window and enter the $C_4F_{10}$ gas volume. Most of the photons reach the sides of the RICH gas containment box. The sides, top, and bottom of the box contain arrays of 3" diameter photomultipliers to detect these photons.

The geometry of the proposed RICH detector is shown in Fig. 4.20. A 3-dimensional representation is given in Fig. 4.21.

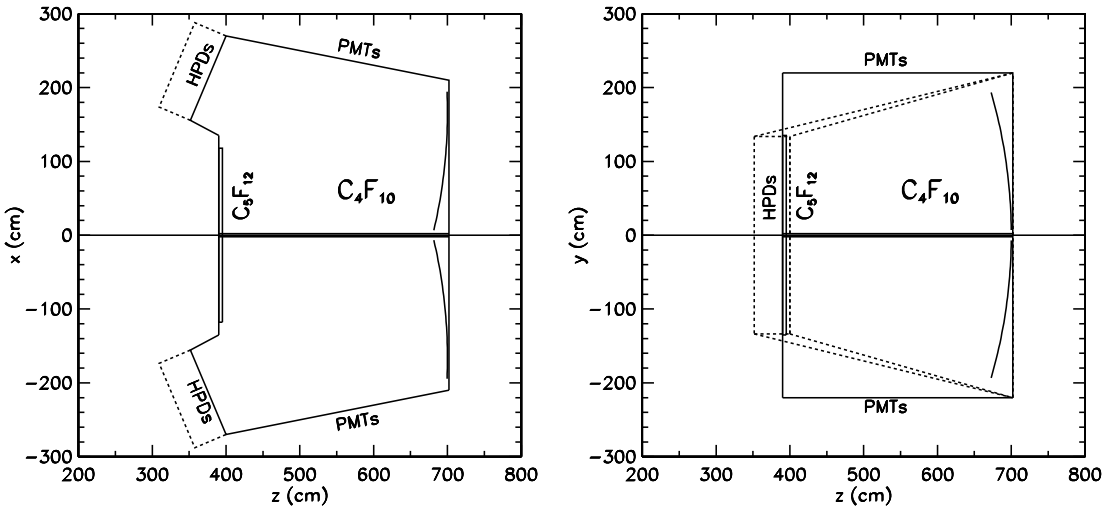


Figure 4.20: BTeV RICH geometry outline. The figure on the left is a plan view and the one on the right is an elevation view. Note the position of the $C_5F_{12}$ on the upstream window and the location of the HPD and photomultiplier sensor planes.

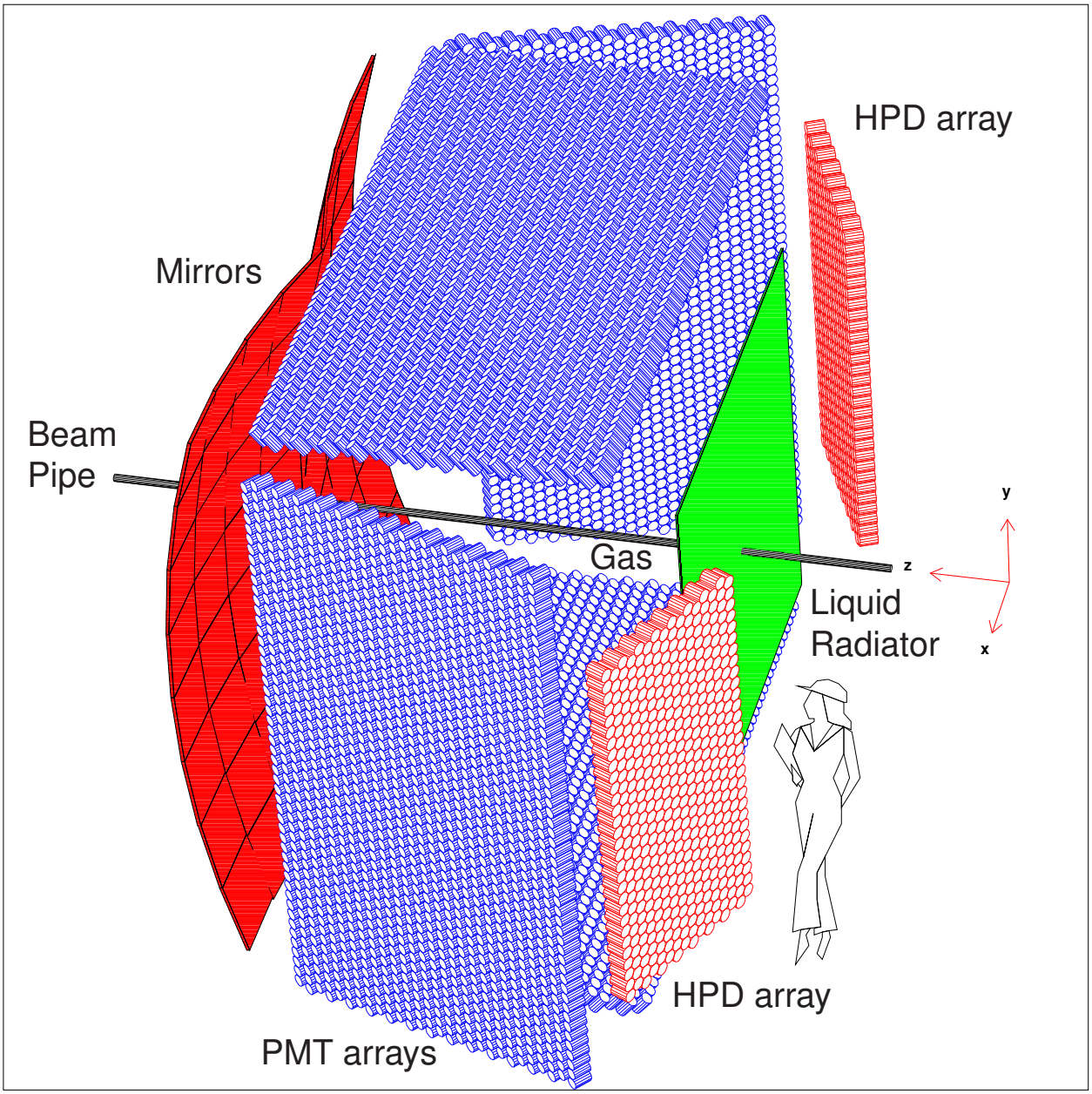


Figure 4.21: Outline of the important RICH components.

### 4.6.4 Photo-detectors

#### 4.6.4.1 Photodetectors for the $C_4F_{10}$ radiator

We choose to work in the "visible wavelength" regime, above 280 nm, to minimize chromatic aberrations (that arise from the wavelength dependence of the radiator refraction index). Because of the open geometry of the forward spectrometer and the availability of space to install shielding to protect detection elements from the fringe field of the BTeV analysis magnet, arrays of photo-multipliers (PMT) or hybrid photo-diodes (HPD) can be used. We chose to use HPDs which offer a cheaper solution. (Multi-anode PMTs are considered a back-up option.)

HPDs are commercially available from DEP (Delft Electronic Products B.V.) in the Netherlands. DEP can now produce pixelated HPDs as large as 8.3 cm in diameter. A photon incident at a quartz window of the HPD refracts and reaches a photo-cathode deposited on the inner window surface. The window has a spherical shape to provide optical focusing of light onto the photo-cathode. About 80% of the tube area is active. Closely packed tubes will cover 91% of the area they occupy, thus the overall geometrical light collection efficiency is 73%. Therefore, there is no need to use any additional demagnification systems to recover the geometric inefficiency.

A photo-electron emitted by the photo-cathode is accelerated onto a segmented silicon diode array by a high voltage ($-20$ kV). The segmentation of the diode array into pixels can be adjusted to match specific spatial resolution requirements. This family of HPD tubes was developed by DEP in collaboration with the LHCb group [12]. Development of BTeV version of the HPD is described in Chapter 5. In the BTeV design we will have 163 hexagonal pixels per tube. The corresponding photon position error is 0.45 mrad.

The gain of the device is about 5000 and is proportional to the accelerating voltage. We expect to detect such signals with a signal-to-noise ratio of about 7:1. Development of the front-end readout electronics is carried out in collaboration with IDE AS company from Norway as described in Chapter 5.

The last major factor impacting the RICH performance is the wavelength coverage determined by the photo-cathode and window material. The wavelength sensitivity determines chromatic error and is the major factor in the number of Cherenkov photons detected per track.

Quartz windows are a standard feature in the HPD tubes as they can easily sustain the large high voltage on the photo-cathode. High quality quartz extends the wavelength coverage from the visible range down to 160 nm. Such a large wavelength coverage results in a large chromatic error of 1.2 mrad per photon and in a large number of photons radiated per track ($\sim 235$). When the wavelength coverage is limited, the photon yield drops but the chromatic error per photon improves. These two effects offset each other. The simulations show that a shallow optimum in Cherenkov resolution per track is reached when the wavelengths are limited to about 280 nm. UVT acrylic used in the vessel window will produce such wavelength cut-off. This results in a chromatic error of 0.45 mrad per photon with a photon yield of 63 photons per track. The total Cherenkov angle resolution is 0.83 mrad per

photon and 0.1 mrad per track.

A system with 944 HPDs/arm approaches the full geometrical coverage limit. With 163 pixels per tube, the detector (1 arm) will have 153,872 electronic channels.

We note that with the replacement of the aerogel with the liquid radiator, the number of HPDs has gone down. With the aerogel, photons struck the mirror and were detected on the HPD array, which had to be enlarged by 96 tubes/arm to capture them. Now, the photons from the liquid radiator are detected on the PMTs on the sides, the top, and the bottom of the counter and the HPD plane only needs to be sized to detect the photons radiated in the $C_4F_{10}$ gas volume.

#### 4.6.4.2 Photodetectors for the $C_5F_{12}$ Liquid Radiator

After passing through the quartz window and refracting on the quartz-glass interface, Cherenkov photons generated in the liquid travel towards the PMT arrays. The PMTs are tilted to match the average angle of incidence. The Cherenkov images at the PMTs are not simple rings since they are distorted by light refraction at the interfaces of the various media and by the orientation of the RICH box's walls. The chromatic error for $C_5F_{12}$ is 3.7 mrad per photon. The emission point error is negligible. The photon position error is determined by the size of the photomultiplier tube. Three inch PMTs produce a photon position contribution to the Cherenkov angle resolution of 5.3 mrad. The total error is then 6.2 mrad. (The total error with 2" tubes would be 4.9 mrad) The current design has 5000 3" PMTs covering the most illuminated portions of the two RICH side walls, the top and bottom. With this system, we expect to detect 12.4 photoelectrons/track, resulting in a per track resolution of 1.88 mrad. Since at 9 GeV/c, kaon and proton Cherenkov angles differ by 5.34 mrad, separation would be 2.8 standard deviations. Separation improves substantially for lower momentum tracks.

Because of the large number of PMTs required, minimizing the cost per PMT is very important. Several companies make 3" PMTs with the required quantum efficiency, gain, noise characteristics, and single photo-electron resolution. Preliminary estimates of radiation levels at the position of the PMTs indicate that radiation damage should not be a problem even after many years of operation.

### 4.6.5 Expected physics performance

In a real environment, Cherenkov rings from different tracks overlap in the detector. A realistic simulation of efficiency and fake rates must take into account ambiguities in track-photon assignment. However, in the new design, the photons from the liquid radiator and the gas radiator fall on separate sensor arrays, which reduces this problem significantly.

We have analyzed simulated data with an algorithm which could be applied to real data. The reconstruction is performed in two steps. In the first pass, all hits within $\pm 3\sigma$ of a mass hypothesis are included in the per track average, excluding those hits which are within $\pm 3\sigma$ of the pion hypothesis for any other track. The second pass is essentially the same except that instead of assuming that all tracks are pions in the hit exclusion, the most likely

Table 4.7: Expected performance of BTeV RICH system. The photon yield and the resolution per track given here do not take into account any reconstruction losses due to overlap of Cherenkov rings from different tracks in the same event. For $C_5F_{12}$, 3" PMTs are assumed.

| | $C_4F_{10}$ $n = 1.00138$ | $C_5F_{12}$ $n = 1.24$ |
|---|---|---|
| emission point error | 0.53 mrad | 0.4 mrad |
| segmentation | 0.45 mrad | 5.3 mrad |
| chromatic error | 0.45 mrad | 3.7 mrad |
| total error per photon | 0.83 mrad | 6.2 mrad |
| number of photons | 63 | 12.4 |
| total error per track | 0.10 mrad | 1.9 mrad |

mass hypothesis based on the first-pass results is used. To discriminate between two mass hypotheses for the same track (e.g. $K$ or $\pi$) we cut on the likelihood ratio expressed as a $\chi^2$ difference: $\Delta\chi^2_{K\pi} = -2\log(L_\pi/L_K)$ with $L_h = P(N_h|N_h^{exp})\,G(\theta_{trk\ h}|\theta_h^{exp})$. Here $P(N_h|N_h^{exp})$ is the Poisson probability for observing $N_h$ photons found within $\pm 3\sigma$ of this hypothesis when $N_h^{exp}$ are expected, and $G(\theta_{trk\ h}|\theta_h^{exp})$ is the Gaussian probability density for obtaining Cherenkov angle per track for given mass hypothesis $h(\theta_{trk\ h})$ when $\theta_h^{exp}$ is expected. The expected photon yield includes acceptance corrections and loss due to the Cherenkov ring overlaps. For a given cut value on the $\Delta\chi^2_{K\pi}$ we obtain a value for efficiency and fake rate.

To illustrate performance of the $C_4F_{10}$ system we show in Fig. 4.22 the updated simulation of $B_d \to K^\pm\pi^\mp$ background rejection as a function of $B_d \to \pi^+\pi^-$ efficiency. The updated simulations include a better description of the detector components which resulted in the increased photon conversion backgrounds. On the other hand, particle discrimination algorithms have been improved. The net change is a slight improvement over the performance curve included in the BTeV proposal.

The gas radiator will play a useful role in lepton identification at low momenta, as its acceptance is much larger than the ones for the calorimeter and for the muon system. This is discussed in more detail in Chapter 2.

To demonstrate the performance of the liquid radiator, we have analyzed Monte Carlo samples of $b\bar{b}$ to show the efficiency and misidentification probability for kaons of momenta less than 9 GeV/c. These are significant in kaon flavor tagging. Background cross-efficiency, in this case the identification of a proton as a kaon, is plotted as a function of kaon efficiency in Fig. 4.23. It should be recalled that with no liquid radiator or, as we have shown with aerogel, we have no discrimination between kaons and protons at these momenta.

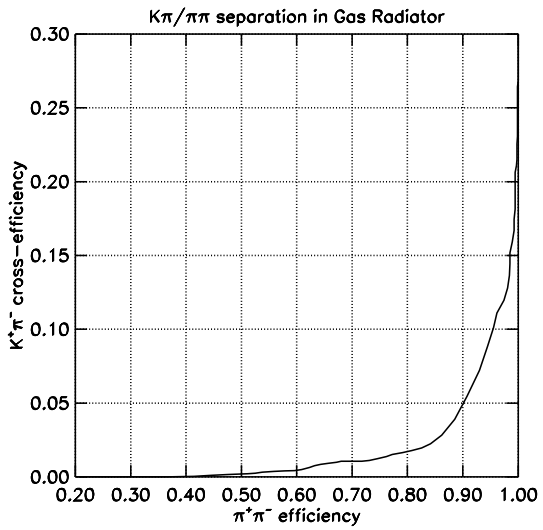


Figure 4.22: Cross-efficiency of particle identification system for $B_d \to K^{\pm}\pi^{\mp}$ as a function $B_d \to \pi^+\pi^-$ PID efficiency. The efficiencies are defined relatively to number of events with both tracks entering the RICH detector. The Monte Carlo simulation included on average two minimum bias interactions in addition to the $b\bar{b}$ production.

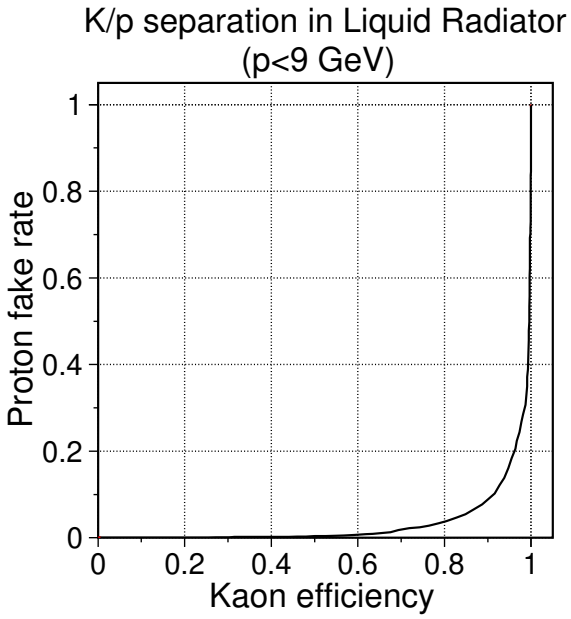


Figure 4.23: Proton fake-rate as a function of kaon identification efficiency for tracks with momenta less than 9 GeV/c.

## 4.7 Electromagnetic Calorimeter

### 4.7.1 Introduction

A thorough investigation of $B$ decays requires the ability to study decay modes containing single photons, $\pi^o$'s, $\eta$'s and electrons. The addition of a high quality crystal calorimeter to the CLEO detector was a first in coupling excellent photon detection to charged particle detection and demonstrated its importance in $B$ decay studies [13]. Furthermore, the identification of electrons is useful to reconstruct $J/\psi$ decays and to identify semileptonic decays, both for their intrinsic physics interest and as "flavor tags" for mixing and CP violation studies.

Some of the important decay modes for BTeV include: $B^o \to (\rho\pi)^o \to \pi^+\pi^-\pi^o$, $B_s^o \to \psi\eta$, and $\psi\eta^{'}$, semileptonic decays, and $B^o \to K^{*o}\gamma$ and $\rho^o\gamma$.

After an extensive study of various technologies, we chose a calorimeter made of $PbWO_4$ crystals. This technology has been developed for high energy physics by CMS. Our choice of lead tungstate is based on several considerations:

- It satisfies our requirements on energy and spatial resolution. Blocks of appropriate transverse and longitudinal size can be manufactured. CMS expects to achieve a stochastic term of 2.7% and a constant term of 0.55% using Avalanche PhotoDiodes (APDs) for readout. We plan to use photomultiplier tubes (PMTs) and expect to have a smaller stochastic term, ∼1.6%-∼1.8%.

- This material is very resistant to radiation damage, especially when doped with either Nb or La. We have verified in test beam runs that these crystals will survive the worst case radiation levels expected in BTeV.

- It is fast – crystals deliver 99% of their light output within 100 ns, which is safely less than the bunch crossing time of 132 ns at the Tevatron.

The properties of $PbWO_4$ which are important for the calorimeter are given in Table 4.8.

### 4.7.2 Description of the BTeV Calorimeter

Our crystals are 220 mm long and 28 mm×28 mm in cross section at the rear face. They are slightly tapered to point towards the interaction region to provide a projective geometry. (They actually project to a point displaced by 10 cm in both the horizontal and vertical direction from the center of the IR to prevent photons from traversing cracks between the crystals.) The crystals are very similar to the crystals used by CMS.

Figure 4.24 shows a representation of the calorimeter, with the crystal hits displayed, for an event generated with GEANT containing a $B^o \to \rho^o\pi^o$ decay. The two photons from the $\pi^o$ decay are indicated by the circles. One photon has 19.3 GeV of energy, while the other has 2.4 GeV. The minimum energy displayed per crystal is 10 MeV. This corresponds to the minimum energy crystal that we use in measuring the shower energy. It can be seen even

Table 4.8: Properties of $PbWO_4$

| Property | Value |
|---|---|
| Density ($g/cm^3$) | 8.28 |
| Radiation Length (cm) | 0.89 |
| Interaction Length (cm) | 22.4 |
| Light Decay Time (ns): | 5(39%) |
| | 15(60%) |
| | 100(1%) |
| Refractive Index | 2.30 |
| Maximum of emission (nm) | 440 |
| Temperature Coefficient (%/$^o$C) | -2 |
| Light output/NaI(Tl) (%) | 1.3 |
| Light output (pe/MeV into a 2" PMT) | 10 |

Table 4.9: Properties of the BTeV electromagnetic Calorimeter

| Property | Value |
|---|---|
| transverse block size, back | 28.0 mm $\times$ 28.0 mm |
| tapered, smaller in front | 27.2 mm$\times$ 27.2 mm |
| Block length | 22 cm |
| Radiation Lengths | 25 |
| Front end electronics | PMT |
| Digitization/readout | QIE (FNAL) |
| Inner Dimension | $\pm$ 9.88 cm $\times$ $\pm$ 9.88 cm |
| Outer Radius | 160 cm |
| Total blocks per arm | 10500 |

from this one event that there is much more activity near the beam line than further out in radius. We will return to this point later.

The light emitted by the crystal peaks at 440 nm. In BTeV, unlike CMS, we are far enough away from magnetic fields, so we can use photomultiplier tubes to read out the calorimeter. BTeV will use modified Hamamatsu R5380 tubes or equivalent equipped with quartz windows to withstand radiation. These are similar to the ones used by KTeV. Using this photomultiplier, we have demonstrated in beam tests conducted at IHEP, Protvino that we can collect approximately 5 photoelectrons per MeV.

The output of the PMT will go to a modified QIE chip [16] located near the photomultiplier base, but outside the region of intense radiation. This chip provides a digitized charge output for each beam crossing. The expected light output is 5000 photoelectrons at 1 GeV. The detector is far enough away from the BTeV dipole so that there should be no need for special magnetic shielding from that source. Since we will magnetize the iron of the muon filter just downstream of the detector, we will put iron shield plates between the

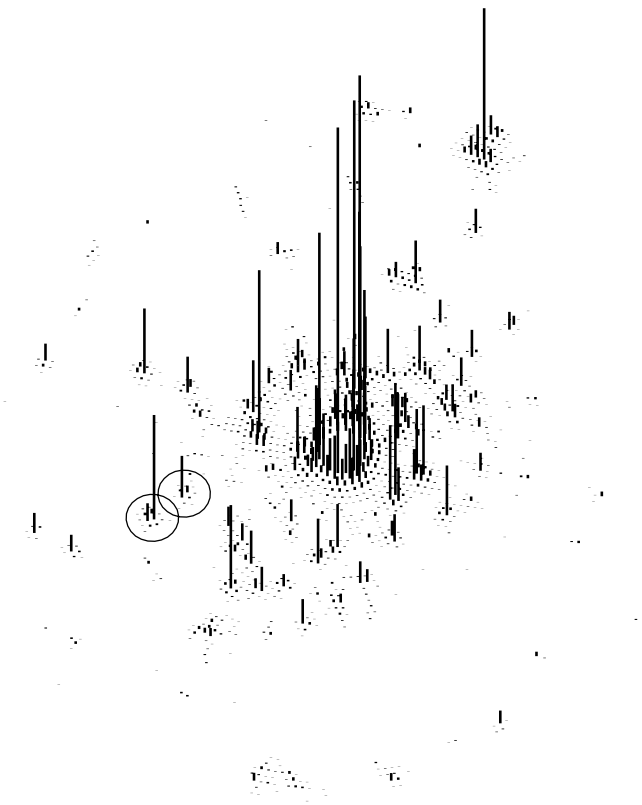

Figure 4.24: The energies in the $PbWO_4$ calorimeter (one arm) for an event containing two photons from the decay sequence $B^o \to \rho^o \pi^o$, $\pi^o \to \gamma\gamma$. The photons of energies 19.3 and 2.4 GeV are surrounded by circles. All energies above 10 MeV are shown, with the height of line proportional to the energy.

calorimeter's PMTs and the muon filter.

The detector will be housed in a temperature and humidity controlled hut. There will be a dry air environment. Temperature stabilization is necessary because of the thermal coefficient of the $PbWO_4$ light output. In addition, the gains will be monitored with a light pulsing system based on Light Emitting Diodes.

### 4.7.3 Radiation Levels and Radiation Tolerance

Radiation damage of PWO crystals is a serious issue. Detailed studies [17] reveal that the light transmission of crystals deteriorates due to formation of color centers by radiation, while the scintillation mechanism itself seems unaffected. When a PWO crystal no longer receives radiation, its color centers (semi-stable excited states) disappear, and it recovers from transmission degradation by natural room-temperature annealing. In fact, this annealing

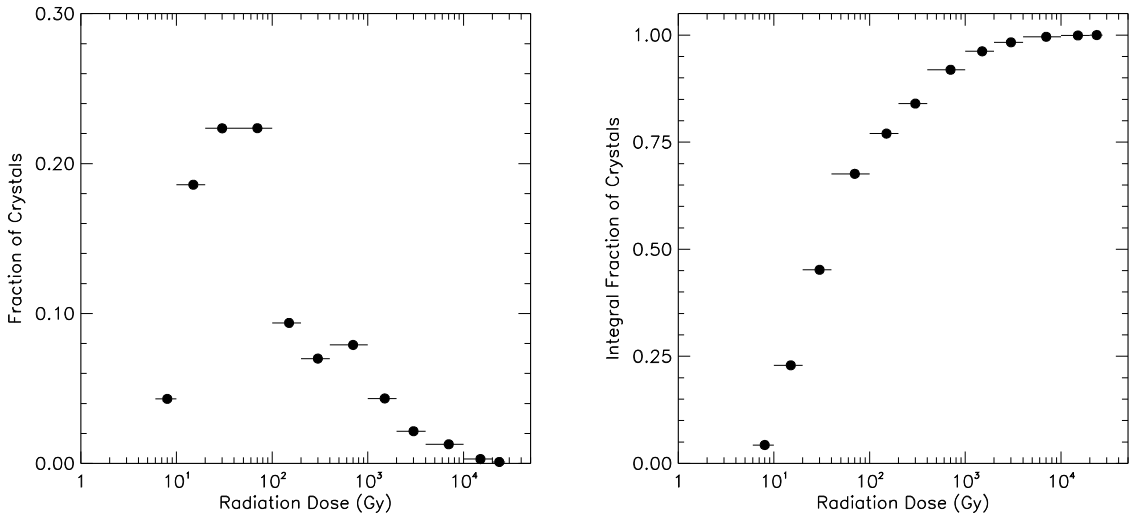


Figure 4.25: (left) The maximum dose distribution in the crystals for for 1 year of running at a luminosity of $2 \times 10^{32}\text{cm}^{-2}\text{s}^{-1}$. (right) The integral of the maximum dose distribution.

goes on even during radiation exposure. Therefore, when crystals are exposed to a constant radiation level, they lose light only up to the point where the rates of radiation damage and natural recovery balance.

The radiation levels at the crystals and phototubes are discussed in Appendix A of the May 2000 proposal. The maximum radiation levels occur close to the beam. There is also a relatively narrow vertical band of higher than average dose caused by the sweeping action of the BTeV dipole.

The simulations shown here were done for a smaller calorimeter of 150 cm radius. The actual outer radius of 160 cm was chosen by weighting the efficiency of a larger calorimeter, up to the spectrometer acceptance of 300 mr, with the cost. The integrated dose rates for most crystals are quite modest. In Fig. 4.25 (left) we show the dose distribution in the crystals (here dose means the maximum dose in any part of the crystals), for 1 year of running at a luminosity of $2 \times 10^{32}\text{cm}^{-2}\text{s}^{-1}$. We also show (right) the cumulative fraction of crystals with doses less than that shown on the horizontal axis. We see that $\sim$90% of the crystals have a yearly accumulated dose of less than 1000 Gy (0.1 Mrad).

The dose rate into most of the BTeV crystals is less than 0.1 Gy/hour, and only a few crystals receive more than 1 Gy/hour. For the 90% of the crystals that are below the lower rate, there are only few percent changes in light output that are easily monitored. At the higher rate, these changes get to the 10% level, but still can be corrected for.

We plan on injecting light from an LED into the crystals for short term monitoring, and have tested such a system in the beam at Protvino (see Chapter 5). Ultimately, we need to use physics events to calibrate every crystal. We plan to use the electron sample from $B$ semileptonic decays as well as converted photons mainly from minimum bias events to

calibrate every crystal. Monte Carlo studies show that there is one electron candidate in every event we record. This implies that there will be $4\times10^6$ electrons every hour, or 200 electrons/crystal for "average"crystals. Although the outer crystals will receive only a few electrons, these crystals won't be effected by radiation either. This implies that for crystals which require careful monitoring of radiation effects, we will be able to calibrate them every hour with electrons.

### 4.7.4 Expected Resolution

The detailed estimates of the expected resolution are given in Appendix A of the May 2000 proposal. Briefly, 22 cm long crystals were selected after a GEANT study determined that length to be optimal. The transverse size was originally chosen to be essentially the same as CMS is already using (26 mm). Making the crystals two mm larger sacrifices little performance and cuts the costs by about 8%, due to a reduced number of photomultiplier tubes and electronics channels.

Using 5 photoelectrons/MeV, we find contributions to the stochastic term in the energy resolution to be $1.5\%/\sqrt{E}$ from photon statistics and $0.7\%/\sqrt{E}$ due to crystal size and clustering (transverse and longitudinal leakage) where $E$ is in units of GeV. For the constant term, we use the CMS estimate of 0.55%. We note that KTeV has achieved a constant term of 0.45% [18]. Overall we expect the energy resolution to be

$$\frac{\sigma_E}{E} = \sqrt{\frac{a^2}{E} + b^2} = \frac{a}{\sqrt{E}} \oplus b, = \frac{1.7\%}{\sqrt{E}} \oplus 0.55\% \tag{4.2}$$

The spatial resolution in both directions transverse to the crystal axis is expected to be

$$\sigma_x = \frac{3500\ \mu m}{\sqrt{E}} \oplus 200\ \mu m\ . \tag{4.3}$$

Our test beam results (see Chapter 5) are consistent with these expectations. With these single photon resolutions, the $\pi^o$ and $\eta$ mass resolutions are excellent. Fig. 4.26 shows the invariant $\gamma\gamma$ mass for $\pi^o$'s of 10 GeV energy incident on the calorimeter. The energies and positions are simulated by GEANT and our cluster finder is used to reconstruct the photons. The mass resolution is 2.6 MeV, which compares favorably to that found in CLEO (5 MeV) [19].

### 4.7.5 Examples: Efficiencies in $B^o \to K^*\gamma$ and $B^o \to \rho\pi$

In the hadroproduction environment, there is great concern that there is so much activity from charged track interactions in the calorimeter and additional photons that the signal photons will be totally obfuscated. As a test case, we use the decay $B^o \to K^*\gamma$. Although we are only concerned with the gamma reconstruction here, we require that the two charged tracks from the $K^*$ decay reach the RICH detector, in order to ensure that the $B^o$'s were

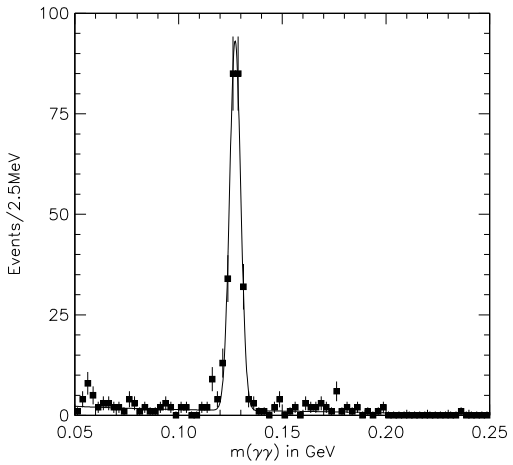


Figure 4.26: The $\gamma\gamma$ invariant mass for 10 GeV $\pi^o$'s incident on the calorimeter. The fit is to a Gaussian signal function plus a polynomial background.

in the acceptance of the spectrometer. The decay was simulated by GEANT at a mean interaction rate of two per crossing.

To identify photons we find clusters of energy whose shape is consistent with an electromagnetic shower and we require that no charged track extrapolate close to the cluster. In Fig. 4.27 we show the difference between measured and generated photon energy divided by the generated energy.

The BTeV energy resolution is about a factor of two better than CLEO. The CLEO spectrum is absolutely clean; there is a small background in the BTeV distribution. Our concern is a large overlap with fragments from other particles that would cause the photon energies to be shifted high and out of the peak, but this apparently is not the case. In Fig. 4.28 we show radial distribution of generated photons from $K^*\gamma$, the accepted ones, and the efficiency; we define accepted photons as ones with energies within $3\sigma$ of the peak that pass the shower shape and isolation cuts. We note that the same number for the CLEO barrel calorimeter, calculated in the same manner using GEANT, is 89%. While our efficiences start out considerably lower than CLEO, they increase rapidly and demonstrate the usefulness of the calorimeter.

We also looked at the $\pi^o$ efficiency as a function of the radius of the $\pi^o$ at the $z$ position of the calorimeter for $B \to \rho^o\pi^o$ and $B \to \rho^+\pi^-$ decays. The efficiency, shown in Fig. 4.29 plateaus at a radial distance of about 75 cm. This simulation was run in a larger than proposed calorimeter so we could view the dependence on radius more easily. From such studies the calorimeter radius was chosen.

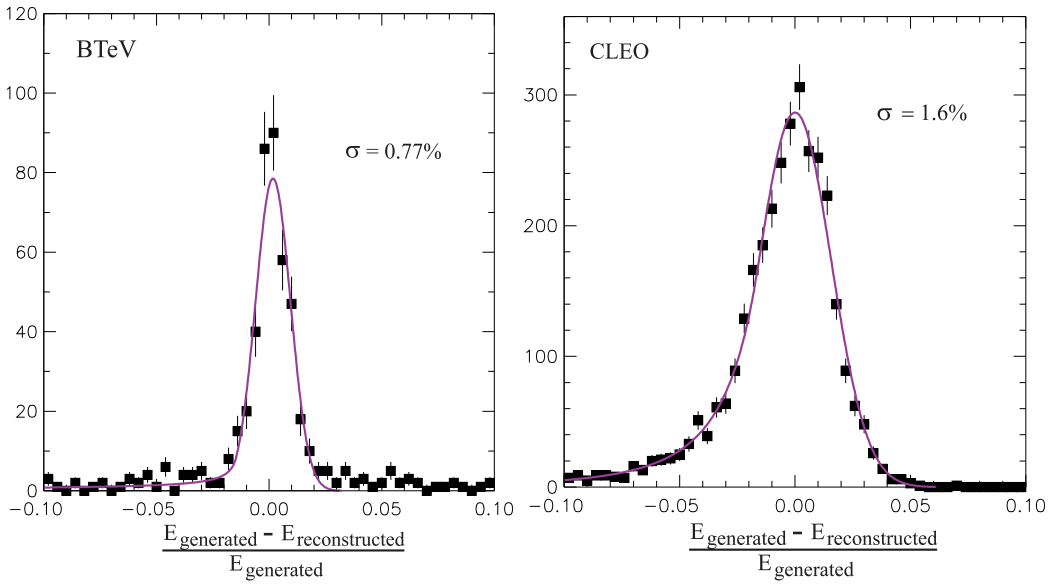


Figure 4.27: The difference between the measured and generated energies, divided by the generated energy, for reconstructed photons as simulated by GEANT for BTeV (left) and CLEO (right). The photons candidate clusters were required to have shower energy shapes consistent with that expected for photons and to be isolated from charged tracks. The BTeV simulation was run at 2 interactions/crossing.

### 4.7.6 Crystal Acquisition

For PWO crystals to be fast and radiation hard, they need to be produced very carefully. Any impurities and crystal defects, such as Pb or O vacancies, increase both the slower components of the light output and the radiation susceptibility. Therefore, establishing mass production procedures to produce good crystals has been one of the major goals of the R&D program of the CMS calorimeter group and its vendors at the Bogoroditsk Plant in Russia and the Shanghai Ceramic Institute.

They have realized this goal by concentrating on the following five factors:

- economical raw material purification methods
- adjustment of the stoichiometric ratio between PbO and $WO_3$ in the raw material to compensate for the evaporation of PbO during crystal growth
- environmental gas during the crystal growth
- annealing methods
- doping with Y, La and/or Nb to compensate residual crystal defects.

The Russian manufacturer uses the Czochralski method to grow crystals. They have already succeeded in producing more than 6000 crystals for the CMS barrel calorimeter.

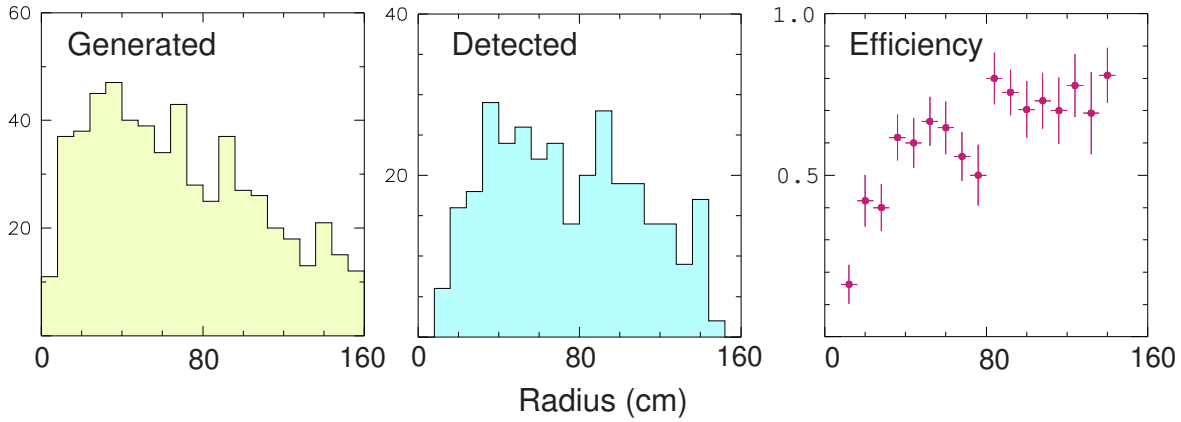


Figure 4.28: The radial distribution of generated and detected photons from $B^o \to K^*\gamma$ and the resulting $\gamma$ efficiency. The detector was simulated by GEANT and the resulting crystal energies were clustered by our software. The charged tracks from the $K^*$ were required to hit the RICH. The simulation was run at 2 interactions/crossing.

They have also completed additional R&D to produce larger endcap crystals, as well as large enough crystals to obtain more than one barrel crystal per ingot, which could lead to lower costs.

The Chinese producer uses the Bridgeman method to grow crystals. Due to prior commitments to other HEP experiments, they started R&D on mass production after the Russians. Nevertheless the Chinese have already produced good sample crystals for BTeV and their quality appears to be comparable to the Russian crystals in our test beam studies.

We have visited both the Bogoroditsk and Beijing/Shanghai production facilties, hosted by our Russian IHEP and Chinese colleagues. We purchased and tested 25 crystals each from Shanghai and Bogorodisk and an additional 12 crystals from the Beijing facility, and are in the process of buying four smaller crystals from a second potential Russian vendor at Apertiti. The two leading companies are interested in growing crystals for BTeV. The Russians plan to finish production for CMS by the middle of 2005 by producing more than 10000 crystals per year. This rate is sufficient to produce the BTeV crystals in one year.

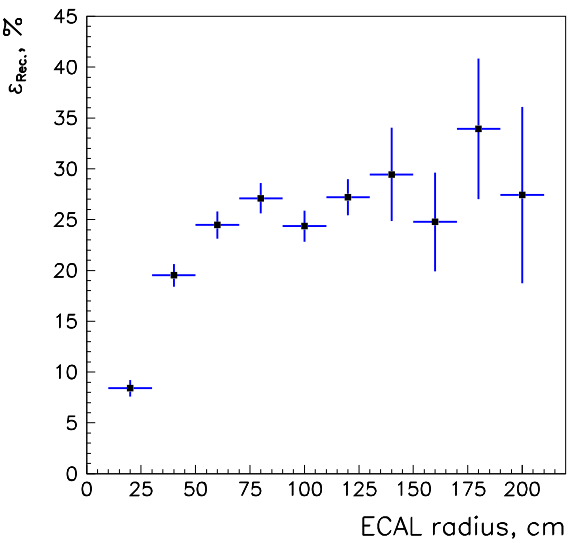


Figure 4.29: The $\pi^o$ efficiency as a function of the radial distance from the beam line in the calorimeter of $\pi^o$'s from $B \to \rho\pi$ decays. The simulation was run at 2 interactions/crossing in the "large" calorimeter.

## 4.8 Muon Detector

The BTeV muon system has two primary functions:

- $J/\psi$ and Prompt Muon Trigger: Besides providing interesting physics (including $J/\psi$ final states of $B$ decays, direct $J/\psi$ production, and semileptonic decays), this trigger performs an important service role by selecting a large enough sample of $b$ events on which the more aggressive and technically challenging vertex trigger can be debugged and its efficiency evaluated.

- Muon Identification: Many of the experiment's physics goals (rare decay searches, CP violation studies which require tagging, studies of beauty mixing, searches for charm mixing, etc.) rely on efficient muon identification with excellent background rejection.

We have selected a toroidal magnet design combined with fine-grained tracking elements. This design permits a "stand-alone" trigger: *i.e.* a di-muon trigger based solely on information from the muon detector. In addition, improved background rejection is possible by comparing this measurement with momentum and tracking information from the rest of the spectrometer. The system design has been chosen to reduce and uniformly distribute occupancies and to minimize confusion in pattern recognition. To provide a viable trigger, the system must obtain a rejection rate at Level 1 of a few hundred. The goal for muon misidentification in the physics analysis is $10^{-3}$.

Given the objective of a stand-alone trigger and the size limitations set by the experimental hall, one can make fairly general calculations that place specific (and restrictive) constraints on the design of the system. We first describe these calculations and use them to motivate the overall design of the muon system. We then describe the trigger efficiency and rejection studies we have performed.

## 4.9 General Design Considerations

The fractional momentum resolution in a magnetic spectrometer can be parameterized as $\sigma_p/p = \sqrt{a^2 + (b\,p)^2}$ where the $a$ term depends on the bending power and multiple scattering environment of the detectors and the $b$ term depends on the bending power and the detector layout and spatial resolution. Figure 4.30a shows that the potential rejection provided by a trigger for low momentum muons significantly degrades once the low momentum fractional resolution exceeds 25%. At $a = 25\%$, the trigger rejects very soft muons at roughly the $4\sigma$ level. At higher momentum, where multiple scattering is less important, one becomes sensitive to the $b$ term. The high momentum resolution influences how sharp a momentum threshold one can make in a stand-alone muon trigger. Figure 4.30b illustrates this point by showing the trigger efficiency as a function of momentum for several $b$ values. These considerations suggest minimum performance criteria of $a < 25\%$ and $b < 1\%/GeV$.

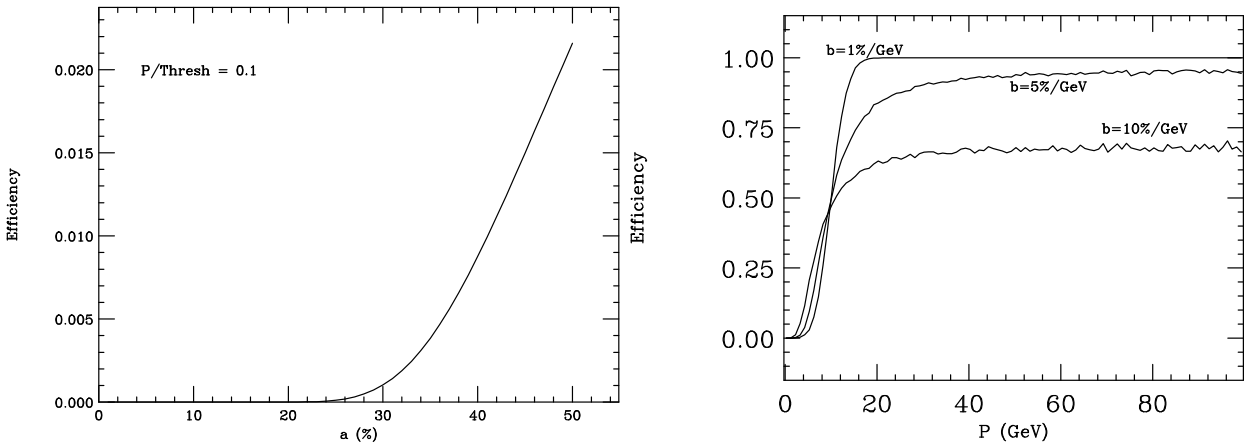


Figure 4.30: (left) Efficiency, calculated in a simple Gaussian model, for a muon with 1/10 the threshold momentum to pass a momentum threshold as a function of $a$, the MCS term in the resolution formula. (right) Efficiency as a function of muon momentum for a trigger designed to fire with a 50% efficiency at 10 GeV. The multiple scattering dominated term is fixed ($a = 25\%$) while the measurement dominated term varies from 1%/GeV$<b<$10%/GeV.

## 4.10 Baseline Muon System

Several measurement and shielding scenarios were studied before reaching the baseline design. In assessing possible layouts, we compute the momentum resolution using an error matrix which incorporates Gaussian models for the detector resolution and multiple Coulomb scattering. The interaction region is modeled as a Gaussian beam spot with $\sigma_x = \sigma_y = 1$ mm and $\sigma_z = 30$ cm. The result of these studies gives us the baseline geometry shown in Fig. 4.31. A cross section of the toriod system is given in Fig. 4.32

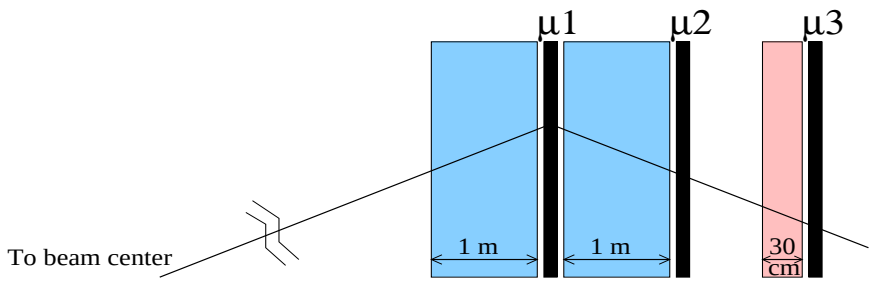


Figure 4.31: Layout of the baseline geometry, shown in elevation view. The three dark boxes, labeled $\mu_1$, $\mu_2$, and $\mu_3$, represent detector stations with 4 measurement views per station. The two lighter boxes with lengths of 1 m represent magnetized steel toroids, which provide bending power for the muon momentum measurement and which also serve as hadron absorbers. The 30 cm long lighter box is an unmagnetized iron shield. The downstream trajectory is measured by $\mu_2$ and $\mu_3$. The upstream trajectory is measured using the nominal beam center with possible help from $\mu_1$. To obtain sufficient bending power, both 1 m steel sections must be magnetized.

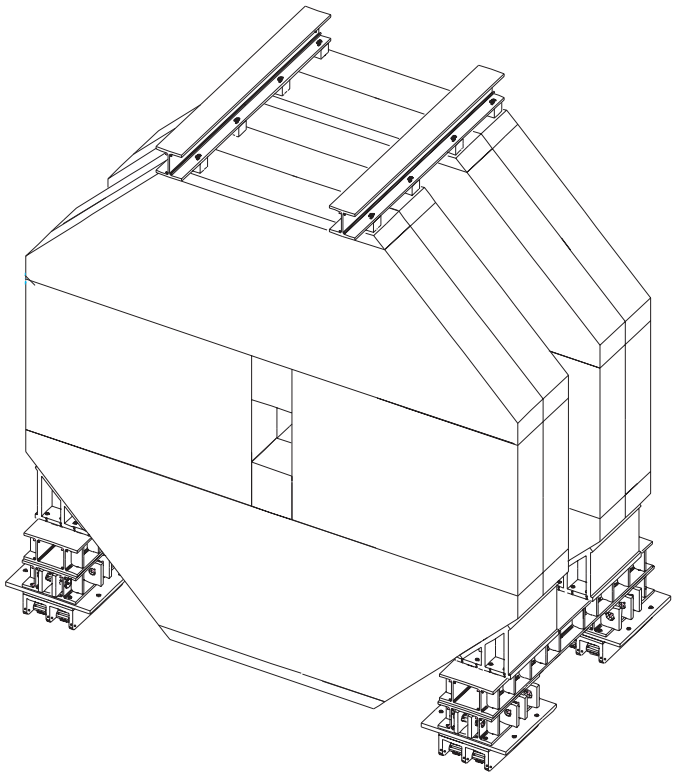

Figure 4.32: Sketch of a Muon Toroid

### 4.10.1 Baseline Geometry

Two toroids, 1 m long with 1.5 T fields, provide the bending power. The muon detectors will be set up in three stations, one between the toroids and two behind the toroids. The momentum can be measured using the two, well shielded, downstream stations and the nominal beam constraint. The station between the two toroids provides a powerful confirming hit to eliminate fake tracks.

The angular acceptance of the muon detector ideally should correspond to the acceptance of the spectrometer, which is 300 mr. However, the physical constraints of the experimental hall do not permit this. The detector radius is chosen to be as large as possible, 240 cm (nearly touching the floor of the enclosure), which corresponds to a polar angle acceptance at the last muon detector station of 200 mr. Fortunately, wider angle muons, which are outside of the acceptance of the muon detector, tend also to have lower energy and can be identified by the Ring Imaging Cherenkov Counter, as discussed above. Muons from $B$ decays which emerge at angles above 200 mr cannot participate in the stand-alone muon trigger described below, but can contribute to the vertex trigger.

There are additional constraints at the inner radius of the detector. The BTeV analysis magnet is part of the Tevatron lattice and deflects the circulating beams. This deflection is compensated by dipole magnets at each end of the C0 enclosure. Moreover, the quadrupoles

that focus the beam at the IR must be as close to the IR as possible. To achieve this, it has become necessary to save longitudinal space by actually inserting the compensating dipoles in the muon toroid as shown in Fig. 4.33. This defines the inner radius of the muon detector to be 38 cm, or about 40 mr. The presence of the magnet coils also creates the potential for particle leakage which must be carefully shielded.

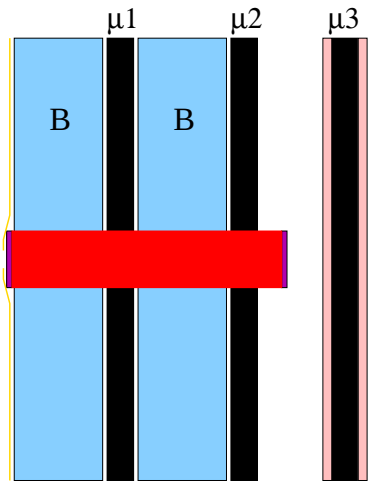


Figure 4.33: Position of Compensating Dipole inside the Muon Toroids

### 4.10.2 Baseline Detector

The basic building block in the construction of a detector station is a "plank" of 3/8" diameter stainless steel proportional tubes as shown in Fig. 4.34. Thirty-two tubes are arranged in a double layer with an offset of half a tube ("picket fence" geometry) and will be soldered at each end to a brass gas manifold and supported in the middle by soldering to brass support rib pieces. This provides a sturdy, self-supporting building block which acts as an excellent Faraday cage. Proportional tubes have been selected as the detector technology because they are robust and have the necessary rate capability. We intend to use a fast gas (*e.g.* 88% Ar, 10% $CF_4$, 2% $CO_2$ ($v_d \approx 9$ cm/$\mu$s) [20]) so the maximum collection time (drift plus charge integration) for a signal should be less than 60 ns, allowing us to gate off hits due to incoming beams which arrive 70 ns before particles from the interaction region. We will use thin walled (0.01") stainless steel tubes. This is a proven technology — it has been used successfully by the CDF collaboration where similar tubes [21] had a long lifetime with low failure rate. The tubes will be strung with 30 $\mu$m gold-plated tungsten wire.

The 0.5 cm wire spacing of this design has no dead regions and has an effective spatial resolution of 5 mm/$\sqrt{12}$ = 1.4 mm which meets the requirements outlined in Section 4.9. Figure 4.35 shows the momentum resolution for various muon system configurations assuming a 2.5 mm resolution and incorporating the magnetic fields and multiple scattering. The top curves show the result for only one magnetized toroid which is clearly ineffective. The

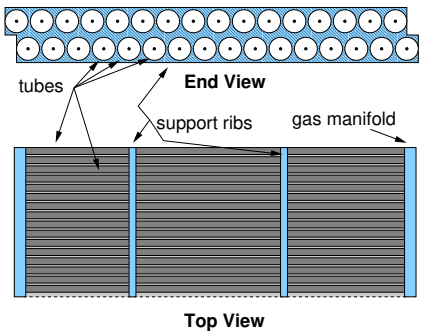


Figure 4.34: End and top views of one "plank" of proportional tubes.

Table 4.10: Parameters of the baseline BTeV Muon System.

| | |
|---|---|
| Radial coverage | 38–240 cm |
| Toroid Z-locations (center) | 870, 1010 cm |
| Average Station Z-location | 940, 1080, 1194 cm |
| Total Length | 4 m (includes toroids) |
| Toroid Length (each) | 1 m |
| Toroidal Fields | 1.5 T |
| Tube cell size | 1 cm (diameter) |
| Wire spacing: | 0.5 cm (staggered) |
| Spatial resolution | 1.5 mm |
| Total channels | 36,864 per arm |
| Momentum resolution | $\sigma_p/p = 19\% \oplus 0.6\% \times p$ |

bottom curves show results when both steel filters are magnetized. The case where only a beam constraint and $\mu_2$–$\mu_3$ are used is illustrated by the dashed red curves. Including information from $\mu_1$ produces the solid magenta curves. Curves are shown for three different azimuths. The chosen geometry exhibits good performance relative to our criteria on $a$ and $b$. The importance of $\mu_1$ lies in providing redundant information to eliminate fake tracks and for matching tracks with the inner tracker at higher trigger levels and offline. Its effect on the momentum resolution is less important.

To minimize occupancy at small radii and to minimize pattern recognition confusion, each detector station will consist of eight overlapping pie shaped "octants," as shown in Fig. 4.36a. The four views ($r$, $u$, $v$, and $r$) in each octant are shown in Fig. 4.36b. The $r$ (radial) view is repeated to provide redundancy for the most important (bend) view and to help reject fake tracks in the trigger. The $u$ and $v$ views are rotated $\pm 22.5^{\mathrm{O}}$ from the $r$ view and are used to measure $\phi$ and to resolve hit ambiguities, thereby reducing the misidentification rate. The views stack on top of each other and are built from the planks described above. There will be 12 planks in each view of an octant. Pairs of octants will be combined into quads which will be the structure moved in and out of the BTeV detector.

A summary of the baseline BTeV muon system is given in Table 4.10.

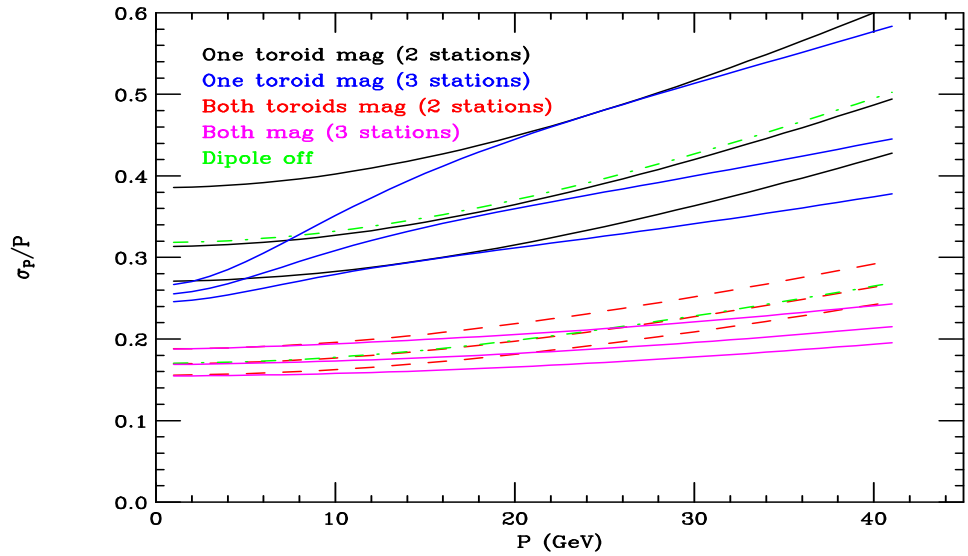


Figure 4.35: Plots of the fractional momentum resolution versus momentum for various muon system configurations. All plots assume 2.5 mm RMS spatial resolution. The plots appear in groups of 3 corresponding to $\phi = 270^o$ (best) $0^o$ and $90^o$ (worst). The $\phi$ dependence illustrates interference between the central dipole and muon toroids. The top (bottom) curves show the resolution when one (two) toroids are magnetized. The black and red curves illustrate the case where only the two stations after the second toroid are used. In this case the trajectory upstream of the toroid comes entirely from the beam constraint. The blue and magenta curves illustrate the case where the station between the two toroids is used to help determine the trajectory prior to the toroids. The green curves assume only the final two stations are used, and the dipole is turned off.

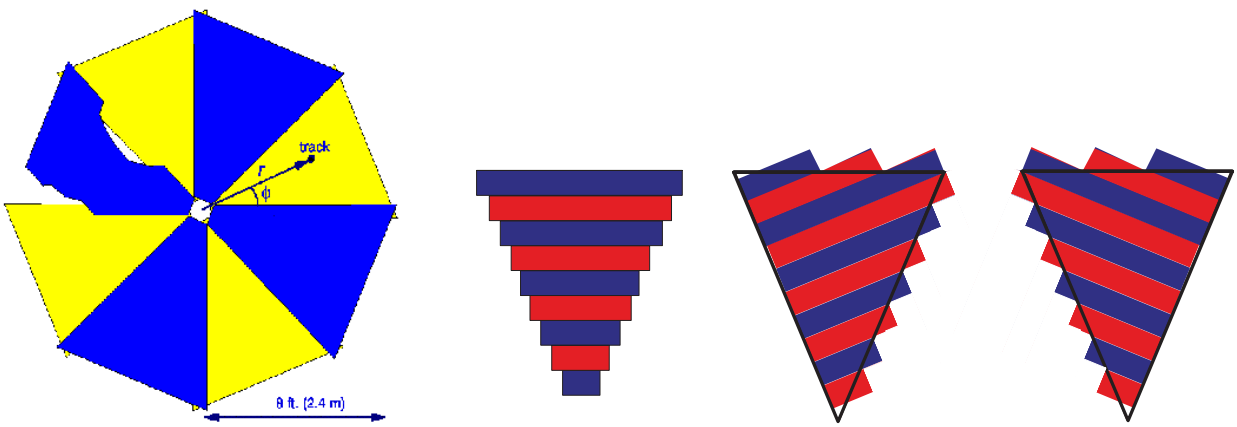


Figure 4.36: (left) Beams-eye view of one muon detector station, which consists of eight overlapping octants arranged in two layers. One octant is cut away in places to show the overlap between adjacent octants. (right) Arrangement of planks to form the four views in an octant ($r$ view is repeated). There will be 12 planks per view (more than shown).

### 4.10.3 Front-end Electronics

Although we will only be reading out a latch bit and not using TDC's, we are considering gating the system to exclude hits coming from the incoming beam. Therefore the front-end electronics need a double pulse resolution $< 30$ ns. The electronics should also be low cost and have sufficient gain. We intend to mimic the setup used for the CDF COT. There will be a PC board to deliver high voltage to each proportional tube, and a PC board with electronics to amplify and digitize the tube signal. Both boards will be located directly at the end of a plank.

We plan to utilize the ASDQ integrated circuit developed at the University of Pennsylvania to amplify and digitize the signals coming from the proportional tubes. This chip is being used in the Run-II CDF central outer tracker for a similar purpose. The ASDQ amplifies the first ∼8–10 ns of the signal and outputs an LVDS (equivalent) differential logic signal. This chip, when mounted on a PC board, has a low effective threshold of about 2 fC and features a double pulse resolution of ∼20 ns. The chip seems to be an ideal choice for the BTeV muon system. Beam tests of the predecessor to the ASDQ, the ASD8B, indicate that it is suitable for our use. Noise problems encountered during the beam test with the ASD8B required creating a Faraday cage out of aluminum, copper plated G10 and copper tape. We will address this problem by completely enclosing the electronics and proportional tube connections in a Faraday enclosure. This is the reason that the gas manifolds (Fig. 4.34) will be made of brass and soldered to the proportional tubes.

The ASDQ digital signals will be sparsified, serialized, and read out using a standard Fermilab readout protocol. Fiber optic cables will transfer the data from the plank to a buffer memory. Slow control and monitoring functions will be performed via fiber optic link as well.

## 4.11 Trigger Studies

We have studied the triggering performance of our baseline muon system using a full GEANT simulation, which includes additional hits in the muon system due to non-prompt sources, $\delta$-rays, electromagnetic shower debris and hadronic shower leakage. We used minimum bias events to study rejection rates and $B^0 \to J/\psi\, K^0_s$ and $B^0_s \to J/\psi\, K^{*0}$ where $J/\psi \to \mu^+\mu^-$, to investigate trigger efficiency. The minimum bias events were generated with PYTHIA and include elastic scattering, single and double diffractive, low $p_T$ scattering and semi-hard QCD $2 \to 2$ processes. The number of events per crossing is generated from a Poisson distribution with average of two. Likewise, in generating the signal events, a Poisson distributed number of minimum bias events (average of 2) were added to the signal event.

### 4.11.1 Properties of additional "noise" hits

Figure 4.37 shows the characteristics of the hits in the muon detector for $B^0_s \to J/\psi\, K^0_s$ events with the original geometry. The noise hits are dominated by low momentum secondaries

coming from interactions with the walls of the beam hole in the muon filters as is evident from the radial position distributions at the downstream faces of the filters. Secondaries spray out of the downstream ends of the holes in both filters. Figure 4.38a documents this problem. The hit distribution in the muon planes can be understood by considering that the percentage of such tracks striking a given plane will increase with the lever arm between the nearest filter and the plane. (All planes go down to the same radial position.) The effect is noticeable in stations 1 and 2 which are just downstream of filters but is largest for station 3. All planes in station 3 receive a large flux due to the long lever arm between this station and the second filter. To reduce this effect we added a 30 cm thick filter with the same radial coverage as the toroids just in front of the third station. The improvement is presented in Fig. 4.38b. Interactions with the beam pipe as well as $\delta$-ray production also contribute significantly to the noise. Additional shielding (8 cm) around the beam pipe is also proposed and the resulting improvement is shown in Fig. 4.38c and 4.38d.

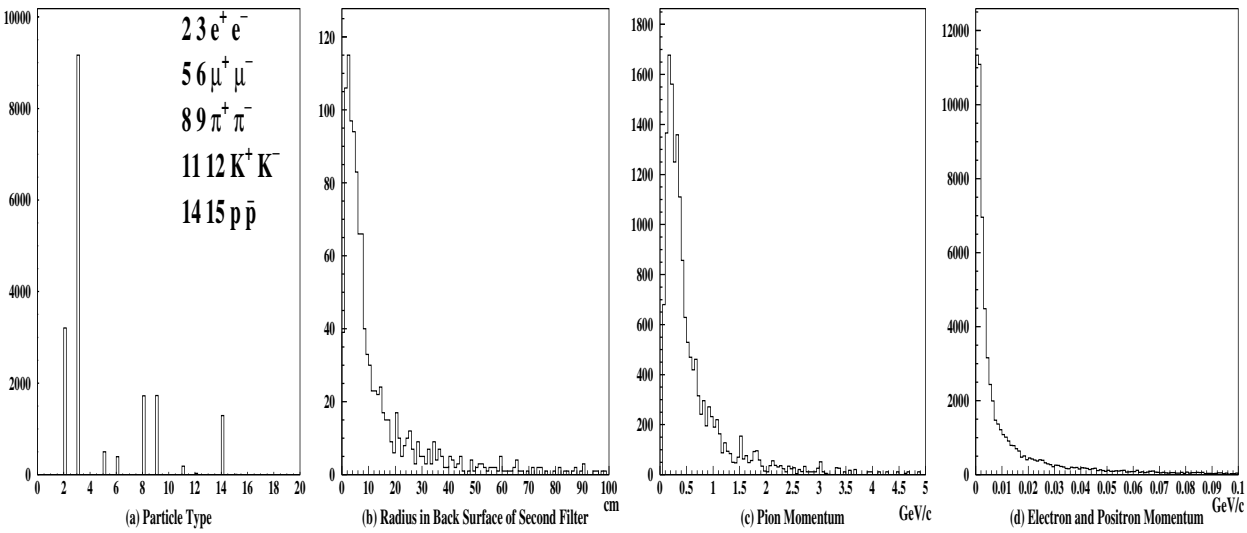


Figure 4.37: Characteristics of muon detector hits for $J/\psi\, K_s^0$ events. (a) Particle type. Each particle type is assigned an integer code, shown in the legend. For example, $\pi^+$ is given the code 8. The electromagnetic and hadronic noise is larger than the muon signal. The excess of electrons over positrons is due to $\delta$-ray production. (b) Projected radial position at the downstream face of the second filter for tracks that hit station 3. The large percentage of tracks emanating from the vicinity of the hole in the filter is quite evident. (c) and (d) Momentum of pion and $e^+/e^-$ noise. Noise secondaries have much lower momentum than $J/\psi$ muons.

### 4.11.2 A muon "tracking" trigger

To establish an "upper" limit on muon trigger performance in the presence of the GEANT generated noise, we studied the performance of a muon "tracking" trigger. This trigger loops over all hits within a given octant to choose the best set of hits using a $\chi^2$ test to the

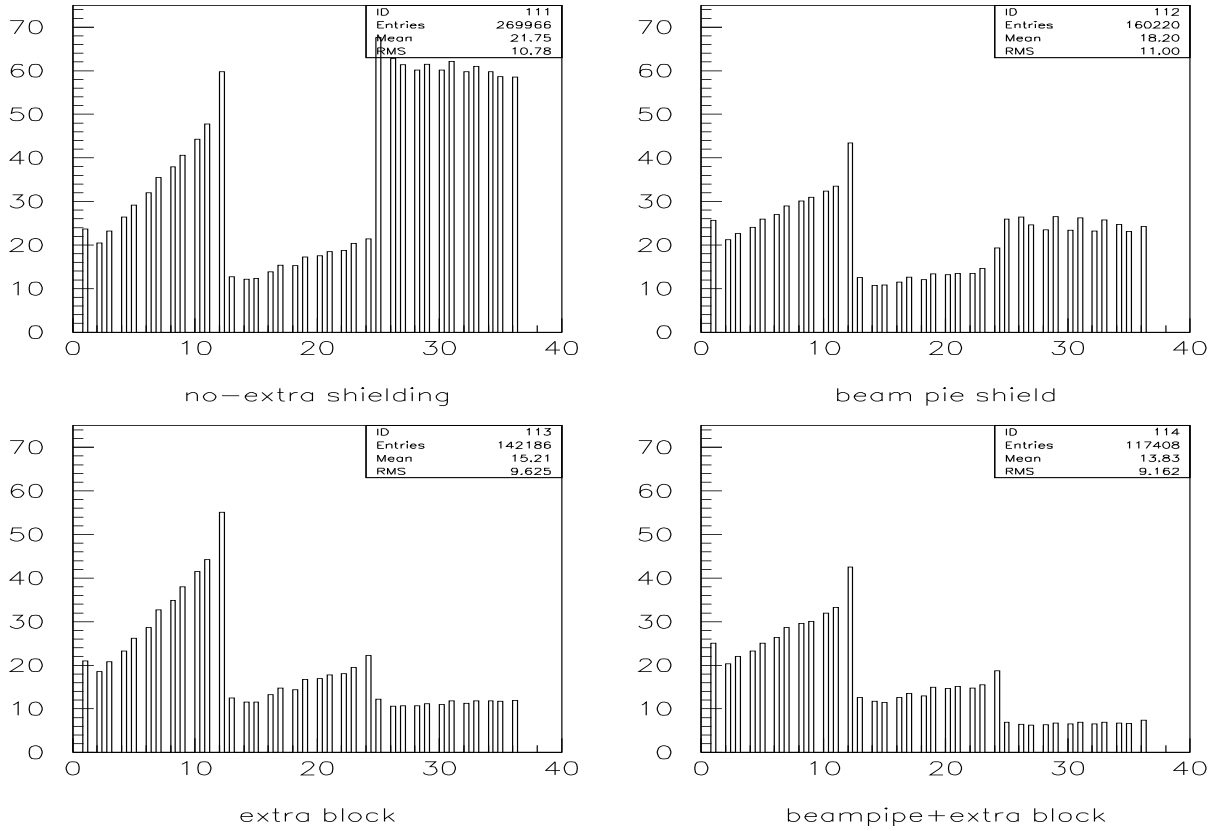


Figure 4.38: Distributions of hits among muon detector planes for different shielding configurations. There are twelve planes per station. (a: upper left) Original design; no extra shielding. (b: lower left) Extra shielding block in front of the third station. (c: Upper right) Extra shielding around the beam pipe. (d: Lower right) Both beam pipe and third station shielded.

hypothesis that the muon system hits form a track which emanates from the nominal beam origin with production angles $x'_o$, $y'_o$, and momentum $p$. It is important to emphasize that this is a simulation of a "stand-alone" trigger. There is no use of any tracking information from the inner tracker; all information comes from the muon system.

For expediency we make several simplifications. We use a significantly simplified magnetic description, and a single bend approximation for the field traces. All equations are linearized in the 3 fit parameters $x'_o$, $y'_o$, and $q/P$ which means that the fit is a classic, non-iterative linear fit. These simplifications keep the number of CPU cycles low and reduce the amount of computing hardware required to execute the trigger.

It is important to note that although the fitting process has been simplified, the GEANT modeling of the muon system has not. A complete magnetic trace is used throughout. Appropriate multiple scattering and $dE/dx$ losses are incorporated. A realistic luminous region is used and non-prompt muons are generated from detached vertices.

Figure 4.39 quantifies the rejection power and relative efficiency of this tracking dimuon

trigger. The $J/\psi$ efficiency is plotted versus the minimum bias rejection ratio. The $J/\psi$ efficiency is normalized to events where both muons from the $J/\psi$ have momentum greater than 5 GeV/$c$ and both muons also leave hits in all three stations of the muon system. All reconstructed muons are required to have $\chi^2 < 25.2$ and the two muons must have opposite reconstructed charge and appear in two different octants. The main branch of the "cut tree" is a requirement on the minimum radius of all the muon hits. Branching off is a set of increasingly tighter cuts on the maximum $\chi^2$. The third branch is a set of cuts on the minimum reconstructed $P_T$.

We are able to achieve a rejection of 600 to 1 with an efficiency of nearly 50% with the principal cuts being a radius greater than 32 cm, a $\chi^2 < 14.4$, and a minimum $P_T > 0.4$ GeV/$c$, although several different cut selections give essentially identical results.

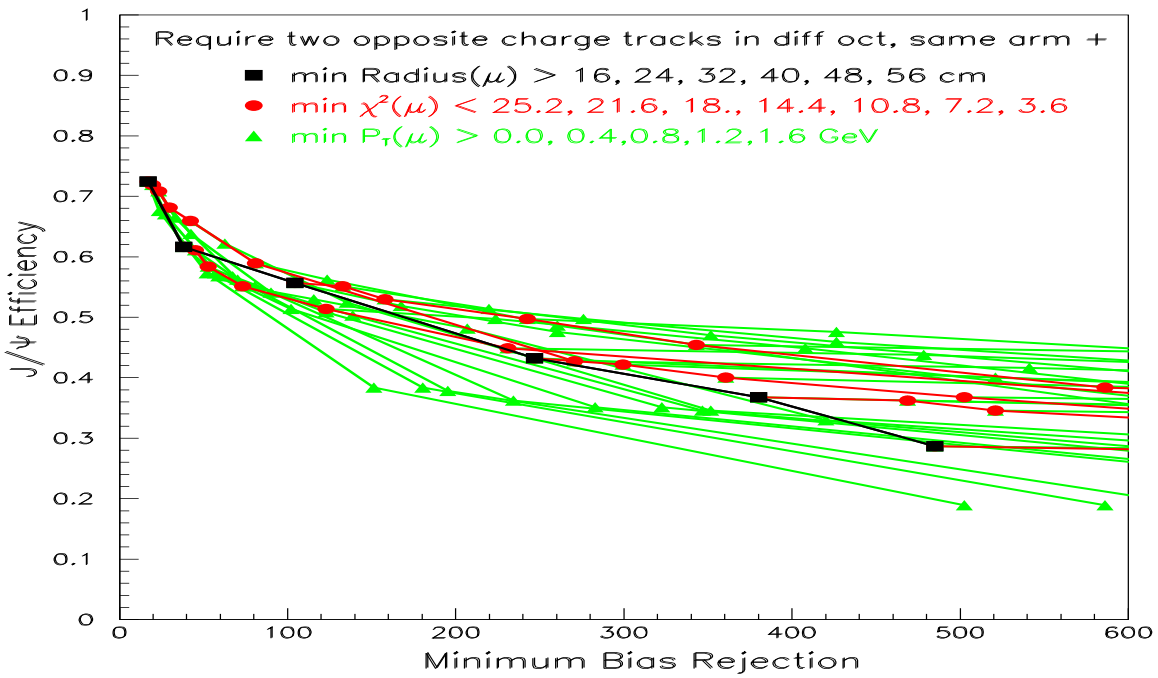


Figure 4.39: $J/\psi$ efficiency versus minimum bias rejection rate for cuts on the minimum radius, maximum $\chi^2$, and the minimum muon $P_T$. Two oppositely charged tracks in different octants in the same arm must pass the relevant cut. Black lines connect the squares which show the variation as the minimum radius is increased. From each black square a red line connecting the circles shows the change as the maximum $\chi^2$ cut is decreased. From each red circle a green line connecting the triangles shows the variation as the minimum reconstructed muon $P_T$ is increased. All information in this stand-alone trigger comes from hits in the muon system alone.

### 4.11.3 Muon Trigger Summary

Using a realistic GEANT simulation, which increases the muon detector occupancy by a factor of 100 with respect to a naive simulation, and the straightforward tracking algorithm

described in Section 4.11.2, we are able to obtain a 600:1 rejection ratio with efficiency of nearly 50%. This trigger will be implemented using a modification of the hardware being developed for the silicon pixel vertex trigger. With a rejection of 600:1, the dimuon trigger uses only a small fraction of the Level 1 bandwidth which is dominated by the vertex trigger, which has a rejection of 100:1. Therefore, this trigger is suitable for both calibrating the vertex trigger and taking physics data. Following the Level 1 trigger (at either Level 2 or Level 3), we can gain further rejection by requiring the tracks which are found by the muon system to correspond to tracks found by the silicon pixels and forward trackers. After requiring a link we can also cut on the more accurate forward-tracker momentum, require the track be detached from the primary vertex, and/or make an invariant mass cut.

## 4.12 The BTeV Trigger System

The trigger system is crucial for the success of BTeV. It finds $B$ events by taking advantage of the main difference between these events and typical hadronic events—the presence of detached beauty or charm vertices. The trigger detects these vertices by utilizing the superior pattern recognition capabilities of the pixel detector to reconstruct tracks and vertices in the first stage of the trigger, Level 1. This is referred to as the Level 1 vertex trigger, which is the primary trigger for the experiment. In addition to the vertexing capabilities of Level 1, the trigger system includes an independent Level 1 muon trigger (described in the previous section) that receives data from the muon detector to select $J/\psi$ and prompt muon events. Besides providing interesting physics on its own, the muon trigger is used to calibrate the vertex trigger.

Results from the Level 1 vertex trigger are combined with results from the Level 1 muon trigger in the Global L1 (GL1) trigger, which ultimately selects the beam crossings that pass the first level trigger. Data that survive the selection criteria are assigned to a Level 2/3 processor for Level 2 analysis. Data that survive Level 2 will be analyzed by Level 3 algorithms that decide whether or not the data should be recorded on archival media.

To perform the large number of calculations needed to process and select $B$ events at a rate of 7.6 million beam crossings per second, we require a massively parallel system with several thousand computational elements. These elements include large Field Programmable Gate Arrays (FPGAs), Digital Signal Processors (DSPs), and general-purpose microprocessors. FPGAs are used at the earliest stage of the processing pipeline to perform large numbers of rudimentary calculations that are required for pattern recognition. DSPs offer more programming flexibility than FPGAs, and are used for the Level 1 trigger calculations that entail track and vertex reconstruction. Moreover, the I/O rate capabilities of DSPs are important at Level 1, since we require high bandwidth to get data to the processors. At Levels 2 and 3 the I/O rate requirements are less critical (data rates are lower than at Level 1), and we have decided to use general-purpose microprocessors for this part of the trigger. The microprocessors provide programming flexibility and significant processing power.

This section provides an overview of the BTeV trigger with references to ongoing trigger R&D described in greater detail in Chapter 5. Many, if not most, of the results for the trigger system presented in the May 2000 BTeV Proposal are still valid today and will not be presented here. One exception is a significant development that promises to drastically reduce the technical risk of the trigger system. Since submission of the May 2000 Proposal, an NSF funded project called RTES (Real Time Embedded Systems) [22] has begun to develop a semi-autonomous, self-monitoring, fault-tolerant and adaptive framework to address issues facing complex computing architectures such as the BTeV trigger. The RTES project is described in Chapter 5.

### 4.12.1 Trigger Overview

The trigger system consists of three levels [23]. Each level contributes to the reconstruction of events, and successive levels impose more and more refined selection criteria to select $B$ events and reject light-quark background events. At Level 1 the trigger reduces the beam crossing rate of 7.6 MHz by a factor of 100 while maintaining high efficiency for $B$ decays that can be successfully reconstructed in the spectrometer. The tracks and vertices found at Level 1 are passed to Level 2. At Level 2 we improve the reconstruction of tracks and vertices by reviewing the pixel data used at Level 1, and by including additional pixel hits in the tracks. At Level 3, all of the data for a beam crossing are available and are used to impose the selection criteria for the final trigger decision. The trigger rate is reduced by an additional factor of 20 by Levels 2 and 3.

As mentioned previously, BTeV will operate at a luminosity of $2 \times 10^{32}$ cm$^{-2}$ s$^{-1}$, corresponding to an average of two interactions per beam crossing at a crossing rate of 7.6 MHz. Average event sizes will be ∼100 KB after zero-suppression of data is performed by front-end detector electronics. Since every beam crossing will be processed, this imposes an extremely high data rate of ∼800 GB/sec on the experiment.

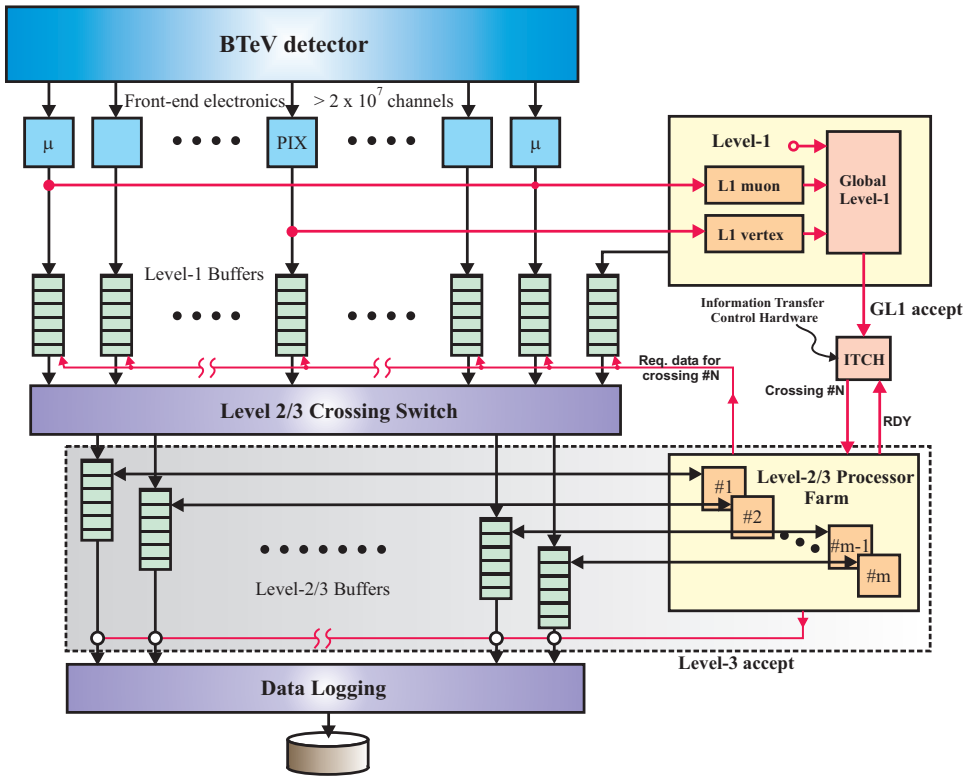


Figure 4.40: BTeV Three-Level Trigger Architecture

BTeV will employ the three-level hierarchical trigger architecture shown in Fig. 4.40, to

handle this high rate. Sparsified data from all detector components will be sent via optical links to Level 1 buffers. Data from the pixel and muon detectors will also be sent to Level 1 trigger processing elements. Trigger results from the Level 1 muon and vertex triggers will be passed on to the Global Level 1 (GL1) trigger manager, where decisions will be stored as a list of accepted beam-crossing numbers by the Information Transfer Control Hardware (ITCH). Level 1 will reject 97.5% of all incoming events, thereby reducing the data rate by a factor of ∼100 to ∼20 GB/sec.

Levels 2 and 3 (L2/3) will be implemented with a cluster of commodity CPU nodes. A request from an idle L2/3 node will be sent to the ITCH, which will respond by assigning a beam-crossing number to that node. This node will then request a subset of the data (mostly pixel data) for that beam crossing from Level 1 buffer managers. A switch will combine data for the same crossing and route them to the buffer of an L2/3 node allowing a more refined analysis that will further reduce the data rate by a factor of ∼10.

If the data satisfy the Level 2 selection criteria, the same processing node will then enter the Level 3 phase and request that data from the rest of the sub-detectors be transferred from Level 1 to Level 3 buffers (L2/3 buffers will simply be the RAM attached to the processing node). Using complete information from the detector, Level 3 will reduce the number of accepted crossings by at least an additional factor of ∼2. We believe that Level 3 will be able to further compress the data for accepted beam crossings by a factor of ∼4, which means that we expect the data rate out of Level 3 to be ∼200 MB/sec.

### 4.12.2 Level 1 Vertex Trigger Algorithm

The first phase of the Level 1 vertex trigger algorithm is the pattern recognition that uses pixel hits to find tracks. This is also referred to as track-segment finding [24]. This phase of the algorithm starts by finding the beginning and ending segments of tracks in two separate regions of the pixel planes, an inner region close to the beam axis and an outer region close to the edge of the pixel planes. The search for the beginning and ending segments of tracks is restricted to these inner and outer regions, respectively. Segments are found using hit clusters from three adjacent pixel stations in the defined regions. Inner segments are required to point back to the beam axis while outer segments are required to project outside pixel plane boundaries. Once these segments are found, they are then matched to form complete tracks in the segment matching stage.

After complete tracks are found, the track and vertex reconstruction phase of the trigger performs calculations to determine the momentum of each track and calculate its transverse distance from the beam axis. Primary vertices are found by looping through all tracks with transverse momenta $p_T \leq 1.2$ GeV/c that appear to originate close to the beam line. Remaining tracks are then tested for their detachment from the primary vertices that were found. The Level 1 vertex trigger selects events if there are at least $n$ tracks in the same arm of the BTeV detector satisfying the following criteria: $p_T^2 \geq 0.25$ (GeV/c)$^2$, $b \geq m\sigma$, and $b \leq 2$ mm, where $b$ is the impact parameter and $n$ and $m$ are tuned to achieve the desired rejection of minimum-bias events. For a single-arm spectrometer we may choose to take

advantage of these selection criteria to select events with $B$ decays that are directed towards the instrumented arm of the spectrometer. This can be done to increase the efficiency for $B$ events in the one-arm spectrometer compared to the two-arm spcectrometer.

Our studies indicate that the Level 1 vertex trigger is able to reject 97.5% of all minimum-bias events while accepting ∼60-70% of the $B$ events that would survive our offline analysis cuts.

### 4.12.3 Level 1 Vertex Trigger Hardware

A block diagram of the Level 1 vertex trigger is shown in Fig. 4.41. Data from all 30 stations of the pixel detector are sent to FPGA-based pixel processors that group individual pixel hits into clusters. Hit clusters from three neighboring pixel stations are routed to FPGA hardware that finds beginning and ending segments of tracks in the pattern recognition phase of the trigger. Track segments found at this stage are sorted by a switch according to their beam crossing number, and routed to a DSP in the track/vertex farm. This DSP performs segment matching, as well as track and vertex reconstruction. Based on initial studies done for the BTeV proposal, we estimated the average processing time per beam crossing for the combined segment matching plus track and vertex reconstruction to take ∼350 $\mu$s on a single 150 MHz TI TMS320C6711 floating-point DSP. Since the time between beam crossings is 132 ns, this would require a total of ∼2,500 DSPs in the track/vertex farm in order to examine every beam crossing. These estimates of our processing needs are compared to real timing results in the trigger R&D section of Chapter 5.

We are currently developing a prototype board for the segment matching, tracking, and vertexing portion of the Level 1 trigger. This prototype has four DSPs so that we can study parallel processing with DSPs. Simulated data will be sent from a host computer to an FPGA buffer manager that distributes the data to each DSP. Reconstructed tracks will be returned to the host computer, trigger results from each processor will be sent through an FPGA interface to an on-board $\mu$-controller and forwarded to GL1, and a second on-board $\mu$-controller will be used as a communications channel to a supervisor and monitor. This allows commands to be sent to the board, initialization of the DSPs, and provides hardware monitoring and fault detection. JTAG ports will be used for real-time debugging and initial start-up of the prototype. More details about the trigger prototype can be found in Chapter 5.

### 4.12.4 Levels 2/3

The Level 2 algorithm refines the tracks found at Level 1 by adding pixel clusters from the planes located between the "inner" and "outer" track segments. It then performs a Kalman-filter track fit, and improves the momentum resolution to about 5–10%. One of two requirements must be satisfied to select an event. A secondary vertex must be present, or the collection of detached tracks must satisfy a minimum $p_T$ cut. The result is a joint light-quark rejection of 1000–1 per beam crossing for Levels 1 and 2 combined and ∼50% overall efficiency

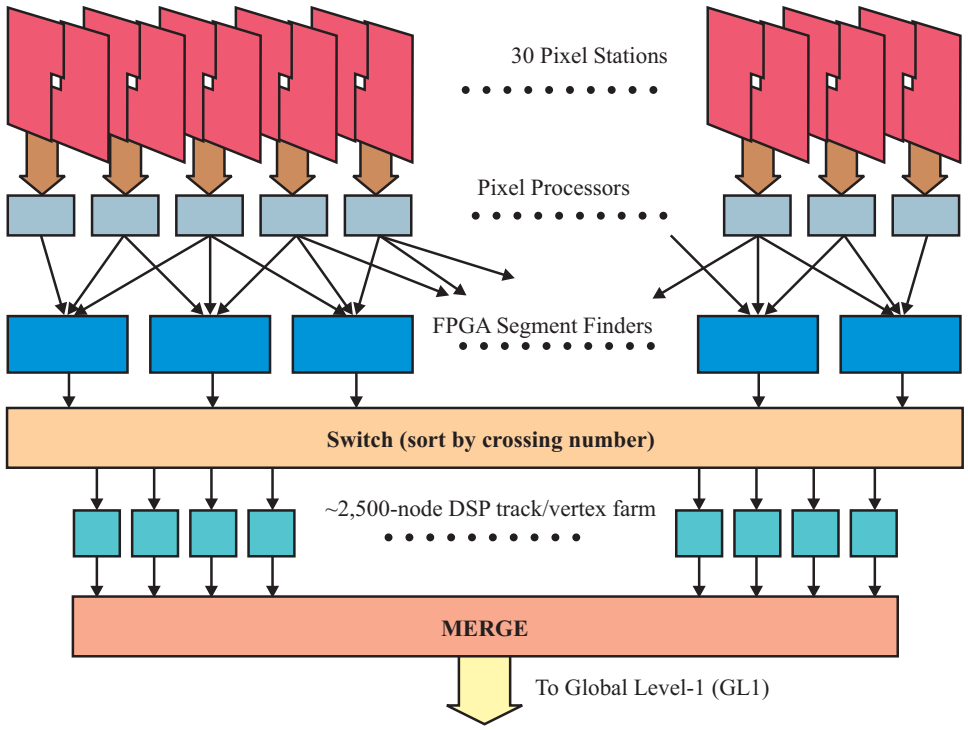


Figure 4.41: BTeV Level-1 vertex trigger.

for most $B$ decays of interest. The execution time of the Level 2 algorithm extrapolates to about 15 milliseconds per beam crossing on the type of processor described below. This performance is sufficient for BTeV operating at the design luminosity. Additional details of improvements made to the algorithms are presented in the trigger R&D section in Chapter 5.

The Level 2/3 trigger is implemented as a farm of commercial processors. These could, for example, be INTEL, PowerPC, or AMD processors running the LINUX operating system. We expect that by the time BTeV runs, processor clock speeds will easily exceed 2.5 GHz. Given an average decision time of 15 ms per Level 2 node, we will need about 2000 of these CPUs.

## 4.13 Data Acquisition System

In BTeV, the Data Acquisition System, the DAQ, and the trigger are intimately connected. To accomodate the BTeV trigger algorithms, which operate asynchronously on beam crossings and do not have fixed latency, substantial event buffering is required at each trigger level and between the final trigger and the system which records the data on mass storage. The function of the DAQ is to transfer data from the detector to the trigger system, provide the buffering and data movement between levels of the trigger system, and from the trigger system to permanent storage.

### 4.13.1 Data Movement between Front End Electronics Boards and Buffer Memories

Preliminary testing indicates that interference problems are minimal when data compression and serialization logic is placed directly on the front-end modules. The baseline design will therefore assume fast serial I/O for all front-end systems.

Data from the front-end electronics is collected by "Data Combiner" boards. The Data Combiners group small data packets from multiple front-end sources into one larger packet, reducing processing overhead in the buffers and switching network. They also route each data packet to one of eight independent branches (or "highways"). The architecture of the trigger and data acquisition ssytem is shown in Figure 4.42. The highway implementation allows the switching network to be built from several smaller commercial switches, instead of one large (possibly in-house developed) switch, at a significant cost savings. Before the data is forwarded to the switching network, it is held in the "Level 1 Buffers" pending the first level trigger decision. More than 97.5% of the events fail the first level trigger and are discarded.

The Data Combiners are currently located near the detector and drive the optical links to the Level 1 Buffers. We are studying the possibility of implementing an asymmetric ring protocol in the front-end module interface so that the Data Combiner function can be moved to the other end of the fiber. This has some potential for cost reduction and improved load balancing. Connections to the front-end boards and from Data Combiners to the Level 1 Buffers will be based, as much as possible, on the emerging 3GIO specification. Connections from the Level 1 Buffers to the switching network will likely be Gigabit Ethernet.

### 4.13.2 Data Buffering for the Level 1 Trigger

The first level trigger is highly parallel, with a significant software component. As a result, the average Level 1 decision time, and the accompanying buffer requirement, are two orders of magnitude greater than in previous systems. The first level trigger also has the distinction of operating asynchronously, which means that the worst-case decision time may be increased by another two orders of magnitude. The BTeV system will digitize, sparsify, and transmit data at the beam crossing rate of 7.6 MHz into off-detector buffer memories. With this approach

applied to all subdetectors, the first level buffers can hold many beam crossings of data and can provide the average latency required for the Level 1 trigger to make its decision. Buffers of this size would be cost-prohibitive if implemented in either analog or digital memory in the front-end ASICs. Commodity DRAM is the only reasonable alternative, with all detector channels digitized at the full crossing rate.

Inputs to the Level 1 trigger are provided by the front end systems over dedicated links. Currently, the pixel detector and muon detector are used in the Level 1 trigger.

### 4.13.3 Data Buffering and Movement from the Level 1 to Level 2/3 Trigger

Three distinct logical trigger levels are described above. From an engineering perspective, there is little difference between Level 2 and Level 3; these levels are both executed in general purpose processors. The only distinction between these levels is that the start of the Level 3 processing presupposes that ALL data have been transferred to the processor, whereas the Level 2 processing operates only on a subset of the total data.

Following the first level trigger decision, which rejects all but 2.5% of the beam crossings, a much more modest volume of approximately 15-20 GBytes/sec must be buffered and eventually transferred to the level 2/3 trigger system. The Level 2/3 trigger is performed with a highly parallel system of commericial microprocessors, which also operates asynchronously with variable latency. The rate is now low enough so that this data movement can be easily accomplished with a commercial switching network. The Level 1 Buffers will include a standard interface and processor, and will appear to the Level 2/3 processors as networked servers. This allows the use of off-the-shelf communications software during the initial implementation. It also supports a variety of access modes, from staged to full transfer of data, under control of the individual L2/3 processors.

The specifications shown in Table 4.11 are used as the baseline for the BTeV data acquisition. These numbers represent both arms of the detector.

| | |
|---|---|
| event size | 100 kBytes |
| number of detector data links | 5000 |
| number of L1 data buffers | 400 |
| number of L2/3 data links | 64 |
| number of L2/3 processors | 2500 |

Table 4.11: Estimates of Hardware for BTeV Trigger and Data Acquisition System

The total system buffer memory, assuming 400 L1/switch input buffers and 64 switch output buffers, is almost 100 Gigabytes. Buffers in the L1/2/3 processors will push total system memory requirement to approximately 400 Gigabytes. We will actually have more than a Terabyte of buffer memory, in case there are unexpected backgrounds or noise.

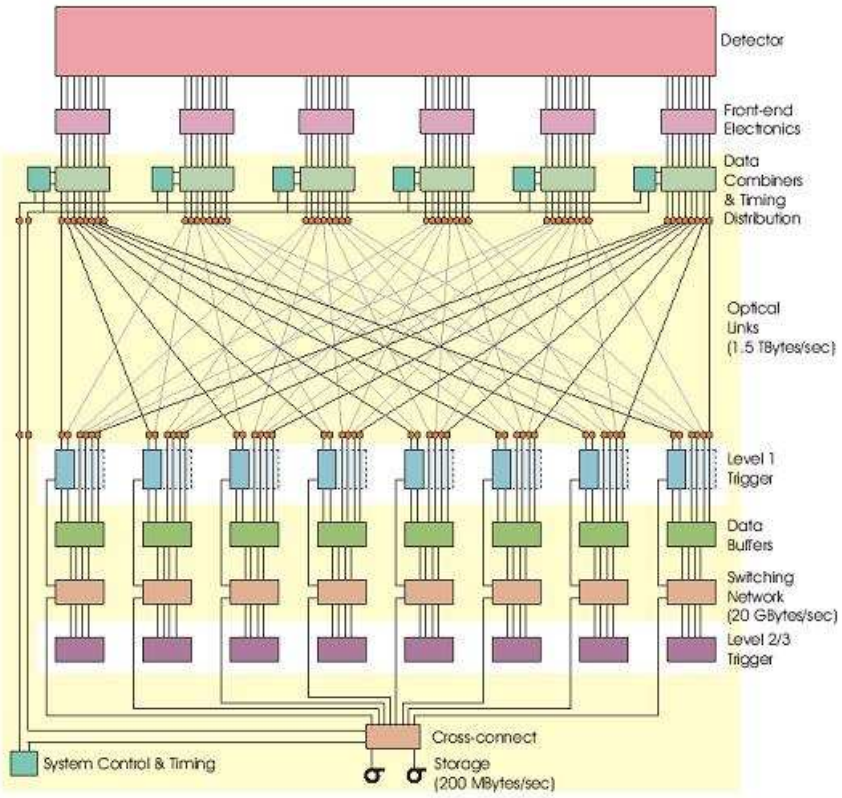


Figure 4.42: Simplified Data Acquisition System showing eight "highways".

### 4.13.4 Data Logging: Movement of Data from the Level 2/3 Processors to Mass Storage Systems

Each event is handled by only one Level 2/3 processor. (i.e., an event is not scattered across processors nor is it copied to more than one processor). All accepted events need to be moved out of the L2/3 processors and onto tape for long term data storage, and a fraction of the events need to be made available for online monitoring (by "consumer processes").

Events coming out of the Level 3 processors will not be raw data, but already processed data (except for a highly prescaled sample used for monitoring the data reduction algorithm itself). This should shrink the event size from 200 kBytes to 50 kBytes. Assuming an event size of 50 kBytes, and a 4 kHz event rate to the loggers, the data rate to tape is on the order of 200 MBytes/sec. The consumer processes will also add an additional 5-10% of throughput.

Since the data logging rate out of each Level 3 processor is small, it is less cost effective to attach logging media to these individual nodes than to provide a small number of separate logger nodes. The necessary bandwidth to the logger nodes is also small (2-3%) compared to the raw data coming up the Level 2/3 farms, so the same switch could be used to pass

the event to the logger nodes as well. Alternatively, a dedicated network could be provided between the Level 3 processors and the logging nodes. In the current plan, a single event is routed to the next free logging node but buffering several events in the Level 3 processors and sending them out together is possible if it turns out to be beneficial.

The number of logging nodes themselves is clearly a function of the data rate. It is assumed that data will first be buffered to disk before being written to tape. This serves a dual purpose; buffering enough data before a transfer to keep the tape drives streaming, and protecting against tape media errors and tape drive failures. With current market technology, a single processor node can handle 10 Mbytes/sec to tape including the initial disk write. We will therefore require a minimum of 20 data logging nodes. We are planning for twice this number to have a safety factor and to be able to handle failures.

### 4.13.5 Slow Control and Monitoring, Hardware Management, and Parameter Control

The data acquisition system also supplies several other key services to the experiment. It includes a slow control and monitoring system, which can initialize, control, and monitor the front end hardware and the components of the trigger and DAQ systems. It can also monitor and, in some cases, control various environmental conditions, such as temperature, humidity, etc. It provides facilities for run control, logging of monitoring and diagnostic information, alarms generation, and the operator interface. These functions are supported by an extensive and sophisticated system of databases, which will provide uniform access to key parameters and permit long term trending and analysis.

# Bibliography


[1] "ATLAS Pixel Detector Technical Design Report", CERN/LHCC 98-13, available at http://atlasinfo.cern.ch/Atlas/GROUPS/INNER_DETECTOR/PIXELS/tdr.html

[2] Y. Arai, *et al.*, "A modular straw drift tube tracking system for the Solenoidal Detector Collaboration experiment, Part I: Design"; Nucl. Instrum. Meth. A 381 (1996) 355.

[3] ATLAS Inner Detector Technical Design Report, CERN/LHCC/97-16,17.

[4] F.M. Newcomer, R. Van Berg, J. Van der Spiegel and H.H. Williams, Nucl. Instrum. Meth. A 283 (1989) 806.

[5] G. Tonelli, *et al.*, "The R&D program for silicon detectors in CMS"; Nucl. Instrum. Meth. A 435 (1999) 109.

[6] M.A. Frautschi, "Radiation Damage Issues for the SVX II Detector"; CDF/DOC/SEC_VTX/PUBLIC/2368.

[7] W. Adam *et al.*, Nucl. Inst. & Meth. **A343**, 60 (1994).

[8] J.L. Rosen, Proceedings of The Fifth International Workshop on $B-$Physics at Hadron Machines, Los Angeles, USA, Oct. 13-17, 1997, published in Nucl. Inst. and Meth. A408 (1998) 191; S. Kopar, Proceedings of the The 3rd International Workshop on Ring Imaging Cherenkov Detectors Weizmann Institute of Science Ein-Gedi, Dead-Sea, Israel, Nov. 15-20, 1998.

[9] P. Carter, Proceedings of the The 3rd International Workshop on Ring Imaging Cherenkov Detectors Weizmann Institute of Science Ein-Gedi, Dead-Sea, Israel, Nov. 15-20, 1998. "Proposal for Dual Radiator RICH for HERMES", E. Cisbani *et al.*, Hermes Internal Note 97-005.

[10] LHC-B, Technical Proposal, CERN LHCC 98-4, LHCC/P4, 1998.

[11] R. Forty, CERN-PPE/96-176, Sept. 1996 published in Proc. of the $4^{th}$ Int. Workshop on $B-$physics at Hadron Machines, Rome, Italy, June 1996, F. Ferroni, P. Schlein (Eds.), North-Holland, 1996.

[12] E. Albrecht *et al.*, "Performance of Hybrid Photon Detector Prototypes With 80% Active Area For The RICH Counters of LHCb", submitted to Nucl. Inst. & Meth. **A**, See also GLAS-PPE-1999-22 (hep-ex/0001053) and Nucl. Inst. & Meth. Phys. Res. **A433**, 159 (1999).

[13] E. Blucher, B. Gittelman, B. K. Heltsley, J. Kandaswamy, R. Kowalewski, Y. Kubota, N. Mistry, A. Bean, and S. Stone, "Tests of Cesium Iodide Crystals for an Electromagnetic Calorimeter," Nuclear Instruments & Methods **A249**, 201 (1986).

[14] We note that a past favorite, CsI (undoped), was attractive from many points of view. However, it is not radiation hard enough. Furthermore, it is not quite fast enough to completely produce all its charge in under one crossing. Lead glass has been rejected because it is not likely to survive the yearly radiation dose.

[15] CMS, "The Electromagnetic Calorimeter Project Technical Design Report," CERN/LHCC 97-33, CMS TDR 4 (1997).

[16] R. J. Yarema *et al.*, A Fast Wide Range Charge Integrator and Encoder ASIC For Photomultiplier Tubes," FEMILAB-PUB-92-311 (1992). This chip was developed for KTEV.

[17] A.N. Annenkov *et al.*, "Systematic Study of the Short-Term Instability of $PbWO_4$ Scintillator Parameters under Irradiation," CMS Note 1997-055.

[18] Private communication from Ed Blucher. The dominant cause of the constant term seems to be a differing crystal response depending on where on the face of the crystal the incident photon strikes. This effect was not observed in the CLEO CsI calorimeter (see ref. 1).

[19] Y. Kubota *et al.*, "The CLEO II Detector," Nuclear Instruments & Methods **A320**, 66 (1991).

[20] J.M. Butler *et al.*, "Study Of Fast Gases, Resolutions And Contaminants In The D0 Muon System," Nucl. Instrum. Meth. **A290**, 122 (1990).

[21] S. Bhadra, S. Errede, L. Fishback, H. Keutelian and P. Schlabach, "The Design And Construction of the CDF Central Drift Tube Array," Nucl. Instr. Meth. **A268**, 92 (1988).

[22] E.E. Gottschalk, The BTeV DAQ and trigger system–some throughput, usability and fault tolerance aspects, Proc. CHEP 2001, Beijing, Sept. 3-7 2001, p. 628.

[23] M.H.L.S. Wang for the BTeV Collaboration, BTeV Level 1 Vertex Trigger, FERMILAB-Conf-01/336-E.

[24] E.E. Gottschalk, BTeV detached vertex trigger, Nucl. Instrum. Meth. A 473 (2001) 167.